Supplementary Information (SI) for Nanoscale.
This journal is © The Royal Society of Chemistry 2025

Electronic Supplementary Information

Electron transport through negatively curved nanographenes

Lucía Palomino-Ruiz,[a,b]* Juan P. Mora-Fuentes,[a] Silvia Castro-Fernández,[a] Irene R. Márquez,[a,c] Juan M. Cuerva,[a] José Catalán-Toledo,[d] Marta Mas-Torrent,[d] Núria Crivillers,[d] Edmund Leary,[b] Alba Millán,[a] Linda A. Zotti,[e,f,g]* M. Teresa González[b]* and Araceli G. Campaña[a]*

a. Departamento de Química Orgánica, Facultad de Ciencias, Unidad de Excelencia de Química Aplicada a Biomedicina y Medioambiente (UEQ), Universidad de Granada, 18071 Granada, Spain.
b. Fundación IMDEA Nanociencia, 28049 Madrid, Spain
c. Centro de Instrumentación Científica, Universidad de Granada, 18071 Granada, Spain
d. Institut de Ciència de Materials de Barcelona (ICMAB, CSIC), Campus de la UAB s/n, Bellaterra 081093, Spain
e. Departamento de Física Teórica de la Materia Condensada, Universidad Autónoma de Madrid, 28049 Madrid, Spain
f. Condensed Matter Physics Center (IFIMAC), Universidad Autónoma de Madrid, 28049 Madrid, Spain
g. Instituto Nicolás Cabrera (INC), Universidad Autónoma de Madrid, 28049 Madrid, Spain

Table of contents:

1. **Synthetic procedures and characterization**
2. **Single-molecule electron-transport measurements and data analysis**
   - **2.1. The break junction technique**
   - **2.2. Experimental details**
   - **2.3. Data collection, processing and analysis**
   - **2.4. Single-molecule conductance for 7-HBC-SMe and HBC-SMe**
   - **2.5. Comparison with 7-HPB-SMe**
   - **2.6. Single-molecule conductance for 7-HBC-alk and HBC-alk**
   - **2.7. Current-Voltage (*I-V*) curves**
   - **2.8 Additional comparison between the two linking groups**
3. **Theoretical calculations**
   - **3.1. DFT-based calculations**
     - **3.1.1. Method**
     - **3.1.2. Gas-phase orbitals**
     - **3.1.3. Local density of states (LDOS)**
     - **3.1.4. Transmission coefficients**
   - **3.2. Tight-binding calculations**
   - **3.3. Additional DFT-based calculations.**
     - **3.3.1. Comparison with 7-HPB-SMe and other molecules**
     - **3.3.2. HBC-alk and 7-HBC-alk in the bridge position.**
     - **3.3.3. The role of curvature vs chemical functionalization**
4. **SAMs preparation and characterization**
   - **4.1. Self-assembled monolayers (SAMs) preparation**
   - **4.2. Cyclic voltammetry characterization**
   - **4.3 Charge transport measurements across HBC monolayers using the "EGaIn technique"**
5. **NMR spectra**
6. **References**

1. Synthetic procedures and characterization

The synthetic route used for the preparation of the heptagon-containing HBC (7-HBC) core, which is shown in Scheme S1, was reported in a previous publications of the group and allows us to prepare compound **1** with good yields.[1] The two brominated positions, which are allocated at opposite edges of the 7-HBC core, permit the π-extension of the structure, but also the introduction of different functional groups, which can play the role of anchors for single-molecule conductance experiments (Scheme S2).

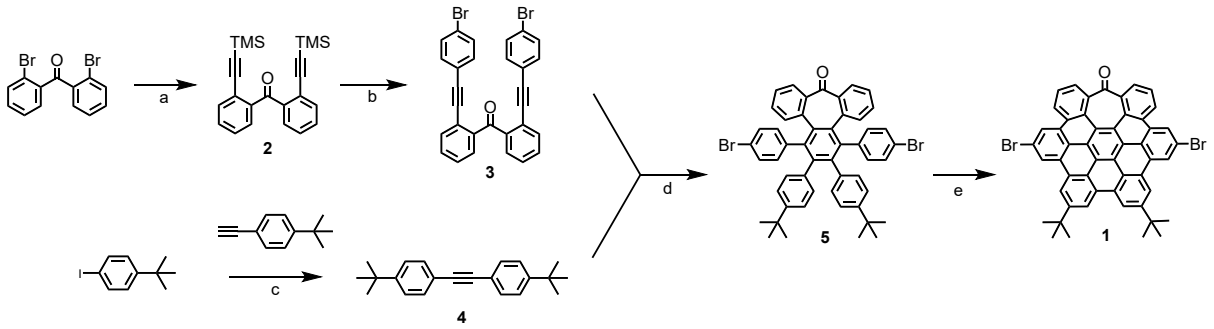

Scheme S1: ***(a)*** *TMSA, $PdCl_2(CH_3CN)_2$, CuI, $PtBu_3{\cdot}HBF_4$, THF, iPr_2NH, rt, 16 h;* ***(b)*** *1-bromo-4-iodobenzene, $PdCl_2(PPh_3)_2$, CuI, Et_3N, DBU, THF, H_2O, 70 °C, 16 h;* ***(c)*** *$PdCl_2(PPh_3)_2$, CuI, Et_3N, THF, rt, 16 h);* ***(d)*** *$Co_2(CO)_8$, toluene, 110 °C, 16 h;* ***(e)*** *DDQ, CF_3SO_3H, DCM, 0 °C, 10 min.*

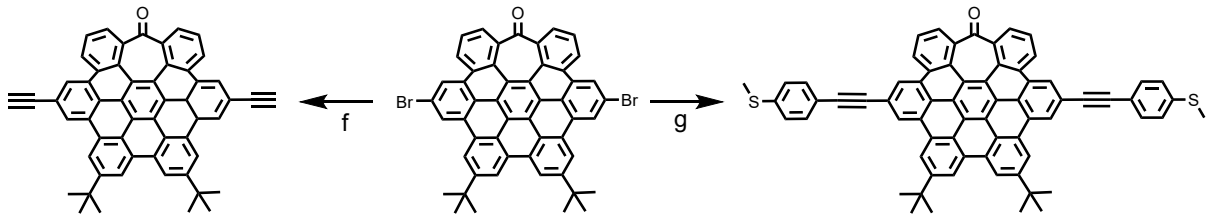

7-HBC-alk **1** **7-HBC-SMe**

Scheme S2: ***(f)*** *(i) TMSA, $PdCl_2(CH_3CN)_2$, CuI, $PtBu_3{\cdot}HBF_4$, THF, iPr_2NH, rt, 16 h; (ii) TBAF, THF, 2 h;* ***(g)*** *(4-ethynylphenyl)(methyl)sulfane, $PdCl_2(CH_3CN)_2$, CuI, $PtBu_3{\cdot}HBF_4$, THF, iPr_2NH, 70 °C, 16 h.*

<u>Synthesis of 7-HBC-SMe:</u>

An oven-dried round-bottom flask was charged with compound **1** (110 mg, 0.135 mmol), Pd $Cl_2(CH_3CN)_2$ (18 mg, 0.069 mmol), CuI (15 mg, 0.078 mmol) and P*t*$Bu_3{\cdot}HBF_4$ (20 mg, 0.068 mmol). The flask was sealed and purged with Ar. Freshly distilled THF (2 mL) and *i*Pr_2NH (6 mL) were added and bubbled with Ar for 10 min. The reaction mixture was heated to 60 °C and a solution of 4-ethynylphenyl)(methyl)sulfane[2] (99 mg, 0.669 mmol) in freshly distilled THF (1 mL) was then added dropwise. The reaction mixture was stirred at 70 °C for 16 h. The mixture was then cooled to room temperature, diluted with DCM and washed with saturated NH_4Cl aq. solution (x2). The organic layer was separated, dried over anhydrous Na_2SO_4 and filtered. The solvent was removed under reduced pressure. The crude was purified by flash column chromatography (SiO_2, Hexane:DCM, 7:3), to give **7-HBC-SMe** (70 mg, 55%). **^{1}H NMR (500MHz, $CDCl_3$)** δ 9.02 (s, 2H), 8.74 (d, *J* = 8.1 Hz, 2H), 8.47 (s, 2H), 8.05

(t, *J* = 7.6 Hz, 2H), 7.99 (bs, 2H), 7.93 (bs, 2H), 7.82 (d, *J* = 8.5 Hz, 4H), 7.79 (d, *J* = 7.4 Hz, 2H), 7.45 (d, *J* = 8.8 Hz, 4H), 2.64 (s, 6H), 1.91 (s, 18H). **^{13}C NMR (126 MHz, $CDCl_3$)** δ 202.4 (C), 149.5 (C), 141.9 (C), 140.0 (C), 132.1 (CH), 129.1 (C), 128.9 (C), 128.7 (C), 127.2 (CH), 126.2 (C), 124.8 (CH), 124.7 (CH), 121.53 (C), 121.46 (C), 121.1 (C), 119.6 (C), 118.7 (CH), 90.9 (C), 35.9 (C), 32.2 (CH_3), 15.5 (CH_3). **HRMS (ESI)** *m/z* calcd for $C_{69}H_{46}ONaS_2$ $[M]^+$: 977.2888; found: 977.2888.

Synthesis of 7-HBC-alk:

An oven-dried round-bottom flask was charged with compound **1** (50 mg, 0.061 mmol), Pd $Cl_2(CH_3CN)_2$ (2 mg, 0.092 mmol), CuI (2 mg, 0,011 mmol) and P*t*Bu_3·HBF_4 (5 mg, mmol). The flask was sealed and purged. Freshly distilled THF (2mL) and *i*Pr_2NH (6mL) were added to the flask. The solution was bubbled with Ar. Trimethylsilylacetylene (TMSA) (90 mg, 0.996 mmol) was added dropwise over the reaction mixture for 30 min. The solution was stirred at room temperature for 16 h. Then, it was diluted with DCM and washed with saturated NH_4Cl aq. solution (x2). The organic layer was separated, dried over anhydrous Na_2SO_4, filtered and the solvent removed under reduced pressure. The crude was purified by flash column chromatography (SiO_2, Hexane:DCM, 2:8). The purified product was diluted in THF (20 ml) with 4-5 drops of water, and tetrabutylamonium fluoride (TBAF) (50 mg, 0.191 mmol) was added. The reaction mixture was stirred and the alkyne deprotection followed by TLC until the consumption of the starting material. The solution was then diluted with EtOAc, washed with brine, dried over anhydrous Na_2SO_4, filtered and the solvent was removed under reduced pressure. The residue was purified by flash chromatography (SiO_2, Hexane:DCM, 35:65) to give **7-HBC-alk** (15 mg, 35%). **^{1}H NMR (400 MHz, $CDCl_3$)** δ 9.03 (s, 2H), 8.57 (d, *J* = 8.4 Hz, 2H), 8.42 (s, 2H), 7.99 (t, *J* = 7.7 Hz, 2H), 7.84 (s, 2H), 7.83 (s, 2H), 7.78 (dd, *J* = 7.3, 1.3 Hz, 2H), 3.56 (s, 2H), 1.90 (s, 18H). **^{13}C NMR (101 MHz, $CDCl_3$)** δ 202.3 (C), 149.8 (C), 141.8 (C), 129.9 (C), 129.02 (C), 128.97 (C), 128.7 (C), 127.5 (C), 127.4 (C), 126.73 (CH), 126.66 (C), 125.2 (CH), 124.9 (CH), 123.5 (C), 123.33 (CH), 123.28 (C), 121.5 (C), 120.1 (C), 119.9 (CH), 119.3 (C), 118.9 (CH), 85.2 (C), 78.8 (CH), 36.0 (C), 32.2 (CH_3). **HRMS (ESI)** *m/z* calcd for $C_{55}H_{34}ONa$ $[M]^+$: 733.2499; found: 733.2507.

The synthetic route used for the preparation of the planar HBCs is showed in Scheme S3. The synthesis up to compound **9** was adapted from literature.[3] Then, two Sonogashira coupling reactions allowed us to obtain **HBC-SMe** and **HBC-alk**.

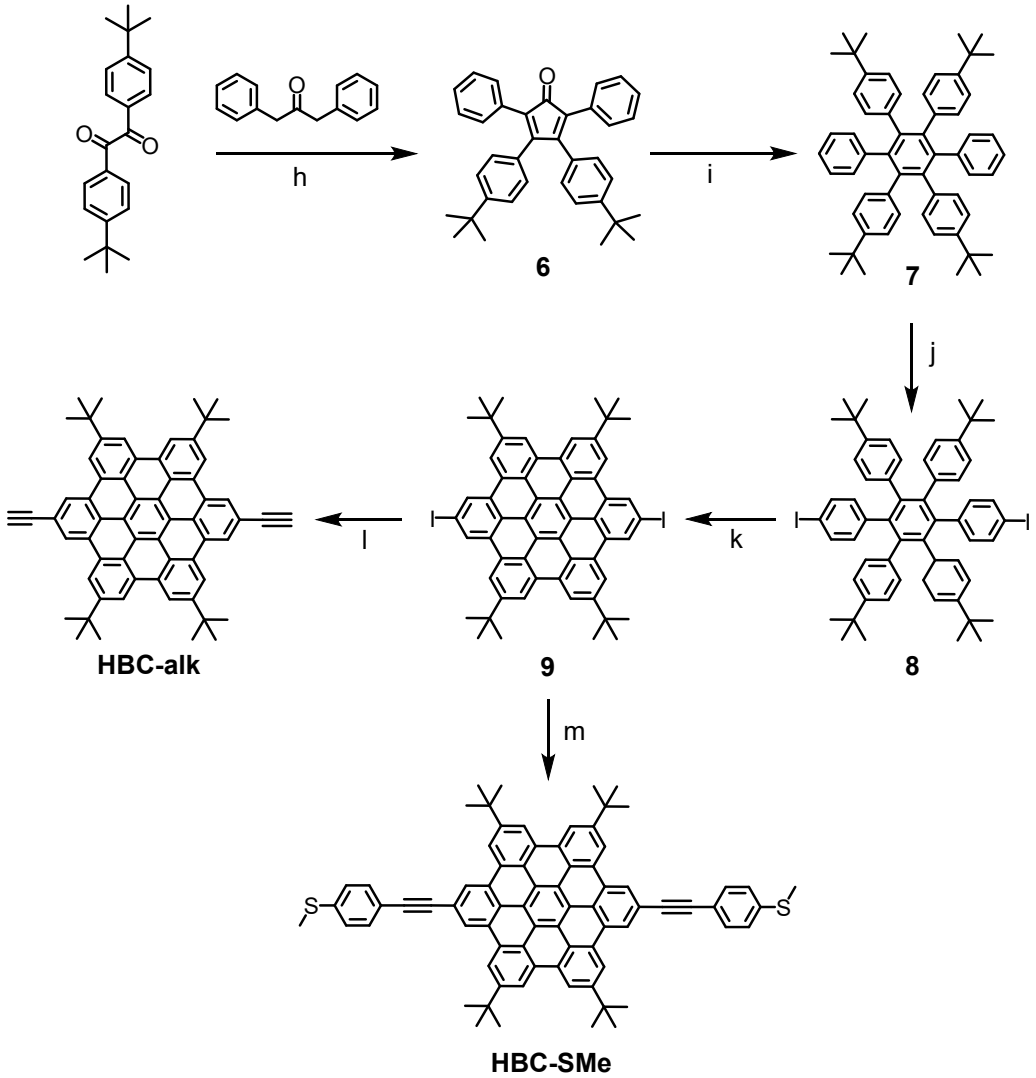

***Scheme S3**: **(h)** KOH, EtOH, reflux, 15 min; **(i)** Ph_2O, reflux, 16 h; **(j)** PIFA, I_2, DCM, rt, 72 h; **(k)** $FeCl_3$, DCM, CH_3NO_2, 0 °C to rt, 16 h; **(l)** (i) TMSA, $Pd(PPh_3)_4$, CuI, Et_3N, THF, 16 h; (ii) TBAF, THF, 2 h; **(m)** (4-ethynylphenyl)(methyl)sulfane, $Pd(PPh_3)_4$, CuI, Et_3N, THF, 16 h*

<u>Synthesis of HBC-alk:</u>

An oven-dried round-bottom flask was charged with compound **9** (20 mg, 0.02 mmol), $Pd(PPh_3)_4$ (2 mg, 0.092 mmol) and CuI (2 mg, 0.011 mmol). The flask was sealed and purged with Ar. Freshly distilled toluene (2 mL) and Et_3N (0.5 mL) were added to the flask and it was bubbled with Ar. The mixture was heated to 60°C and TMSA (24 mg, 0.24 mmol) was added dropwise for 30 min. The reaction mixture was stirred for 16 h at 60 °C. Then, it was diluted with DCM and washed with saturated NH_4Cl aq. solution (x2). The organic layer was separated, dried over anhydrous Na_2SO_4, filtered and the solvent removed under reduced pressure. The crude was purified by flash column chromatography (SiO_2, Hexane:DCM, 1:1). The purified product was diluted in THF (20 mL) with 4-5 drops of water, and TBAF (50 mg, 0.191 mmol) was added. The reaction mixture was stirred and the alkyne deprotection

followed by TLC until completion of the reaction. The solution was then diluted with DCM, washed with brine, dried over anhydrous Na_2SO_4, filtered and the solvent was removed under reduced pressure. The residue was purified by flash chromatography (SiO_2, Hexane:DCM, 7:3) to give **HBC-alk** (11 mg, 70%). **^{1}H NMR (400 MHz, $CDCl_3$)** δ 8.96 (s, 4H), 8.62 (s, 4H), 8.57 (s, 4H), 3.67 (s, 2H), 1.94 (s, 36H). **HRMS (MALDI)** *m/z* calcd for $C_{62}H_{50}$ $[M]^+$: 795.3995; found: 795.3990. A good-quality ^{13}C-NMR could not be obtained due to poor solubility of the compound.

Synthesis of HBC-SMe:

An oven-dried round-bottom flask was charged with compound **9** (100 mg, 0.1 mmol), Pd $Cl_2(CH_3CN)$ (2 mg, 0.092 mmol) and CuI (2 mg, 0.01 mmol). The flask was sealed and purged with Ar. Freshly distilled toluene (8 mL) and *i*Pr_2NH (6 mL) were added to the flask and it was bubbled with Ar. The mixture was heated to 60°C and (4-ethynylphenyl)(methyl)sulfane (100 mg, 0.5 mmol) in THF (3mL) was added dropwise for 90 min. The reaction mixture was stirred for 16 h at 60 °C. Then, it was diluted with DCM and washed with saturated NH_4Cl aq. solution (x2). The organic layer was separated, dried over anhydrous Na_2SO_4, filtered and the solvent removed under reduced pressure. The crude was purified by flash column chromatography (SiO_2, Hexane:DCM, 7:5) to give **HBC-SMe** (60%). **^{1}H NMR (600 MHz, $CDCl_3$)** δ 8.89 (s, 4H), 8.56 (s, 4H), 8.48 (s, 4H), 7.84 (d, 4H), 7.43 (d, 4H), 2.61 (s, 6H), 1.90 (s, 36H). **^{13}C NMR (101 MHz, $CDCl_3$)** δ 147.9 (CH), 139.7 (CH), 132.2 (C), 129.6 (C), 128.9 (C), 126.2 (C), 124.4 (C), 123.8 (C), 122.2 (C), 119.1 (C), 118.8 (C), 118.7 (C), 35.8 (CH_3), 32.4 (CH_3), 15.5 (C). **HRMS (MALDI)** *m/z* calcd for $C_{76}H_{62}S_2$ [M]: 1038.429; found: 1038.4286.

The synthetic route towards the heptagon-containing oligophenylene analogue (**7-HPB-SMe**) is described in Scheme S4.:

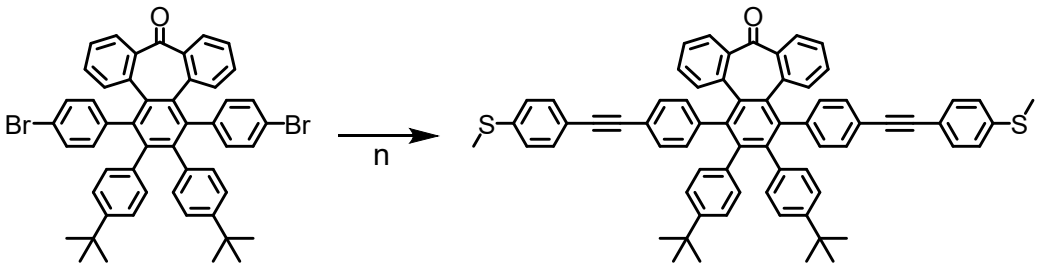

5 **7-HPB-SMe**

***Scheme S4*: (n)** *(4-ethynylphenyl)(methyl)sulfane, $PdCl_2(CH_3CN)_2$, CuI, $PtBu_3{\cdot}HBF_4$, THF, iPr_2NH, 70 °C, 16 h*

Synthesis of 7-HPB-SMe:

An oven-dried round-bottom flask was charged with **5** (85 mg, 0.102 mmol), $Pd(CH_3CN)_2Cl_2$ (8 mg, 0.030 mmol), CuI (7 mg, 0.037 mmol) and P*t*$Bu_3{\cdot}HBF_4$ (9 mg, 0.031 mmol). The flask was sealed and purged with Ar. Freshly distilled THF (2 mL) and *i*Pr_2NH (4 mL) were added and bubbled with Ar for 10 min. The reaction mixture was heated to 70 °C and a solution of 4-ethynylphenyl)(methyl)sulfane (40 mg, 0,270 mmol) in freshly distilled THF (1 mL) was then added dropwise. The reaction mixture was stirred at 70 °C for 16 h. The mixture was

then cooled to room temperature, diluted with DCM and washed with saturated NH_4Cl aq. solution (x2). The organic layer was separated, dried over anhydrous Na_2SO_4 and filtered. The solvent was removed under reduced pressure. The crude was purified by flash column chromatography (SiO_2, Hexane:DCM, 8:2), to give compound **7-HPB-SMe** (30 mg, 31%). **^{1}H NMR (400 MHz, $CDCl_3$)** δ 7.42 (d, *J* = 7.7 Hz, 2H), 7.36 (d, *J* = 8.4 Hz, 4H), 7.20-7.08 (m, 12H), 7.02–6.94 (m, 6H), 6.88 (t, *J* = 7.6 Hz, 2H), 6.67 (d, *J* = 8.1 Hz, 2H), 6.47 (d, *J* = 8.0 Hz, 2H), 6.24 (d, *J* = 8.1 Hz, 2H), 2.48 (s, 6H), 1.07 (s, 18H). **^{13}C NMR (101 MHz, $CDCl_3$)** δ 200.3 (C), 148.3 (C), 146.0 (C), 143.4 (C), 141.1 (C), 140.9 (C), 139.2 (C), 136.7 (C), 135.3 (C), 134.7 (C), 133.2 (CH), 132.5 (CH), 131.8 (CH), 131.3 (CH), 130.7 (CH), 130.5 (CH), 129.8 (CH), 129.7 (CH), 128.9 (CH), 127.3 (CH), 125.9 (CH), 124.3 (CH), 123.8 (CH), 122.8 (CH), 120.1 (C), 119.6 (C), 89.8 (C), 88.9 (C), 31.1 (CH_3), 15.4 (CH_3). **HRMS (ESI)** *m/z* calcd for $C_{69}H_{56}ONaS_2$ $[M]^+$: 987.3698; found: 987.3670.

2. Electron-transport measurements and data analysis

2.1. The break junction technique

The break-junction experiments are based on a push-pull process between the STM electrodes. After pushing the STM tip and substrate into contact, the tip is pulled upwards, and the current between both electrodes decreases in a stepwise fashion. These steps correspond to quantized units of $G_0=2e^2/h$, which means that the metallic contact size is decreasing in only one Au atom from one step to the next. A last plateau at G_0 forms when the contact between the electrodes consists of just one gold atom. Additional plateaus appearing at $G<G_0$, indicate that one or a few molecular bridges have been formed between the electrodes and the conductance value of the plateau is assigned to the conductance of the molecular junction.

2.2. Experimental details

The break-junction experiments were carried out with a STM designed and built in house, which works at air and room temperature. We used freshly cut gold wires (Goodfellow) as tip and commercial gold on quartz samples (Arrandee) as substrates. Before the preparation of the samples, the substrates were cleaned with ethanol and flame-annealed. Later, the substrates were immersed for 15-20 min in dichloromethane solutions of the target molecules, with concentrations between 10^{-4} and 10^{-3} mM. Finally, they were dried with nitrogen gas.

A made-in-house linear current-to-voltage (*I*-*V*) converter with two stages of amplification was used for obtaining the conductance-distance (*G*-*z*) traces. The gains, of $1\cdot10^8$ Ω and $3.5\cdot10^{10}$ V/A respectively, were selected according to the conductance values observed for the compounds under study. These values allowed us to explore a range in conductance $G=I/V$ of 8 orders of magnitude between 10 G_0 and 10^{-7} G_0. A protection resistor of $2\cdot10^6$ Ω was placed in-series with the STM circuit.

For the conductance measurement (*G*), a constant 0.16 bias voltage was applied between the electrodes, while recording thousands *G*-*z* traces for each molecule.

For the Current-Voltage (*I*-*V*) curves, a current ramp was applied along the molecular plateaus at selected conductance ranges, according to the width of the molecular peak obtained in the conductance 1D histograms (detailed information about the histograms is included in the following section).

2.3. Data collection, processing and analysis

Several rounds of thousands of *G*-*z* traces were collected for each compound, changing to new tips, substrates or even different product batches in order to ensure the reproducibility of results. The data analysis started with the conductance-distance alignment of the traces. We used as the origin for the *z* axis the point where the conductance of the traces reached to 0.5 G_0. This value corresponds with the moment just after the last gold atom in the contact is broken. As molecular junctions do not occur in all the *G*-*z* traces, those traces presenting plateaus were separated from those displaying merely a drop in the tunnel

current, using an automatized program. The criterion for considering a trace containing plateau is that, at any conductance below 0.5 G_0, a displacement Δz larger than 0.1 nm is needed to produce a change in conductance of $\Delta\log(G/G_0) = 0.1$. As reference, the typical displacement needed for that conductance change for gold−gold tunneling in air is 0.02 nm.

From this separation process, it is also possible to obtain the rate of success to form molecular junctions from all recorded breaking events (percentage of traces containing plateaus).

1D and 2D conductance histograms were built from all the traces displaying plateaus. We built 1D histograms by accumulating the number of points N_{points} measured in fixed $\log(G/G_0)$ intervals. The y-axis in these histograms is normalized, as follows:

$$N_{\text{norm}} = N_{\text{points}} / (N_{\text{curves}} \cdot v_{\text{p}} \cdot \Delta\log(G/G_0))$$

where N_{curves} is the total number of *G-z* traces included in the histogram, and v_p is the number of points recorded per unit of length in *z*.[4] With this normalization, N_{norm} is now just the inverse of the typical $\log(G/G_0)$ *vs z* curve. This tells us the distance *z* that we would need to move to produce a variation of 1 order of magnitude in conductance *G*, at each particular point. Therefore, it has units of nanometers per order of magnitude that we abbreviate to nm/order-mag. At those conductance values where the *G-z* traces display plateaus, there will be a larger number of points, and a peak will form in the 1D conductance histograms. For extracting the experimental typical conductance value for the molecular junctions of each compound, a Gaussian distribution has been fitted to the corresponding peaks in the 1D histograms. The main value of the curve is the most probable conductance value, while the error is given as the half width at half maximum (HWHM) of the Gaussian fit. The wide of this peak can change depending on the nature of the anchoring groups and the molecule skeleton. Particularly broad or asymmetric peaks can appear when i) multiple molecules are involved in the junction, ii) when multiple processes are occurring during the junction breaking; and iii) when different molecule orientations in the junction are possible at close G values. In these cases, the breaking profile displayed in the 2D histograms are also difficult to analyze, and an additional clustering-based analysis has been applied to separate individual traces into different groups, depending on different breaking profiles. This process is detailed later in the text.

We built 2D conductance-distance histograms by accumulating the number of points $\boldsymbol{N_{points}}$ measured in fixed $\log(G/G_0)$ and *z* intervals from the traces. In this case, a color scale from green to brown was used for displaying the $\boldsymbol{N_{points}}$, where green represents the *G-z* intervals with fewer number of points and brown represents the *G-z* intervals with higher number of points.

The length of the plateaus was calculated as the variation of *z* (Δz) needed to change the junction conductance from 0.5 G_0 to a conductance value below the peak observed in the corresponding conductance histogram. The plateau length was obtained for every individual trace, and then plateau-length probability, *p*, distributions were calculated using the data of all traces displaying plateaus. The tail of the probability distribution usually corresponds to the expected maximum plateau length for the junction, only obtained in a disposition when the molecule is fully extended between the electrodes. Other conformations for the molecule in the junction are also possible, but giving rise to shorter plateaus. In addition, it is also often to obtain shorter plateaus when the molecule loses connection with one of the

electrodes before reaching the extended configuration while the breaking process. When this happens, the most probable plateau-length is always shorter than the expected one. The theoretical or expected values are calculated as the theoretical molecular distance between the linking points, namely from the middle Au–L bond of one side to the other, once an interval of 0.4 nm is subtracted to compensate the electrode retraction promoted by the gold relaxation after the contact breaks.[4] Therefore, the comparison of this value with the experimental maximum plateau length permits to check that the conductance signal is not due to oligomeric forms, and even elucidate the molecule geometry in the junction.[5] Both, the theoretical distance and the expected maximum plateau length for the molecules under study are collected in Table S1.

Table S1. Calculated distances for junctions of the molecules under study, their corresponding estimated maximum value for the plateau-length and their experimental and theoretical conductance values, discussed along the article.

Compound	Linker-linker (nm)	Au/atom bond (nm)	Expected maximum plateau-length (nm)	Experimental conductance (log G/G_0)	Theoretical conductance –DFT– (Go)
7-HBC-SMe	2.54	0.24	2.38	–6.0	1.6×10^{-5}
HBC-SMe	2.75	0.24	2.59	–6.0	1.1×10^{-5}
7-HBC-alk	1.55	0.21	1.36	–3.0 (A) –3.5 (B)	1.32×10^{-4}
HBC-alk	1.59	0.21	1.40	–2.9 (A) –3.5 (B)	1.64×10^{-4}

For the molecules under study, an additional clustering-based method has been applied in order to distinguish different breaking profiles present in the set of molecules containing plateaus. We transform each *G-z* trace into an image, more specifically into a 2D histogram. Then, each 2D histogram is converted into a feature vector, obtaining as many vectors as individual breaking curves. Depending on the molecule under study, a specific region of interest is defined (a conductance range between the noise value and G_0, and an electrode displacement range according to the calculated junction distance for the molecule fully extended between the electrodes) in order to reduce as much as possible, the high-dimensional spaces that are generated. The feature vectors are then separated in groups according to their profiles in the selected area.

Current-voltage (*I-V*) characteristics has been also studied in molecular junctions by means of applying voltage cycles while the molecule is wired between the electrodes; this is, while the molecular plateau in the *G-z* trace remains. The treatment of *I-V* curves is similar to that described for *G-z* traces. Thousands of current-voltage cycles are recorded, generally several of them in each plateau that appear in the *G-z* traces. The 2D histograms are built from all these *I-V* curves. The behavior of the *I-V* curves is generally related to the HOMO-LUMO gap, so the higher the curvature of the *I-V*s, the closer in energy the HOMO or LUMO are with respect to the Fermi level.

2.4. Single-molecule conductance for 7-HBC-SMe and HBC-SMe

The 1D and 2D histograms obtained from all the traces containing plateaus for these molecules can be found in Figure 2 in the main text. In this section, only the clustering-based analysis is shown.

For both molecules, the clustering-based analysis allowed us to differentiate three groups of *G-z* traces according to their breaking profiles (Figure S1). The first group (panels a and e) corresponds to traces displaying broken plateaus. These traces are formed when the molecule-electrode interaction is reached during the stretching process of the electrodes. In these traces, the molecular plateau is observed only after a signal jump from the noise to the molecular conductance value. This kind of plateaus are especially useful for determining the most probable conductance of the molecule with high accuracy, since the presence of only one molecule in the junction is ensured. The three other groups correspond to continuous traces, but presenting different breaking profiles. The second group (panels b and f) is formed by traces displaying flat and long plateaus in the same conductance range. As revealed by the plateau-length distributions, the maximum plateau length obtained for these two first groups is quite similar. This maximum is in agreement with the expected maximum length for the plateaus, which is 2.5 nm and 2.4 nm for **HBC-SMe** and **7- HBC-SMe**, respectively (see Table S1). The third group (panels c and g) is formed by traces displaying shorter plateaus, but at the same conductance range than those in the second group. The plateau-length distribution for this group of traces is quite broad (Figure S2, panel d), going from 0.5 to 1.75 nm, and has its maximum at 1.1 nm. Finally, the fourth group (panels d and h) corresponds to inclined plateaus starting at higher conductance values. This group of traces could be due to junctions presenting more than one molecule between the electrodes, or by dynamic breaking processes with the molecule sledding along the electrodes during the stretching.[6] In both cases, the latter is the minority group.

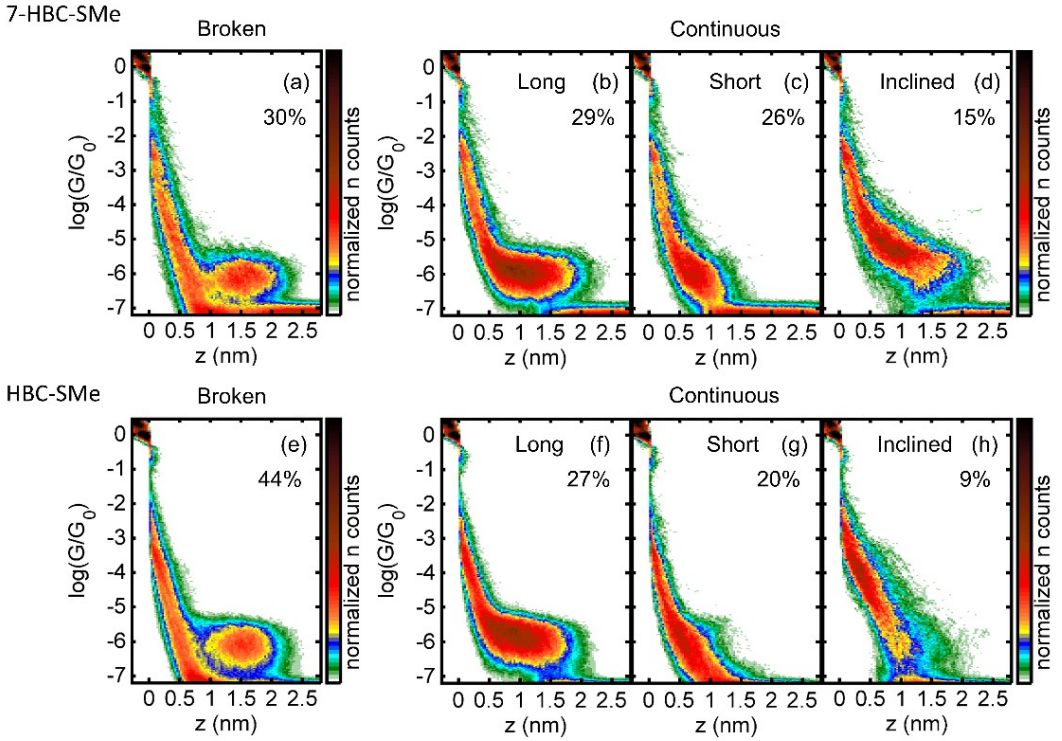

Figure S1. 2D histograms of the four groups of *G-z* traces differentiated by the clustering-based analysis of **(a)-(d) 7-HBC-SMe** and **(e)-(h) HBC-SMe** *G-z* traces. The percentages indicated in the panels refer to the percentage of *G-z* traces used in each 2D histogram respect to the total number of recorded *G-z* traces that display plateaus. No significant differences are observed either in the shape of the histogram or the probability of each group for the two compounds.

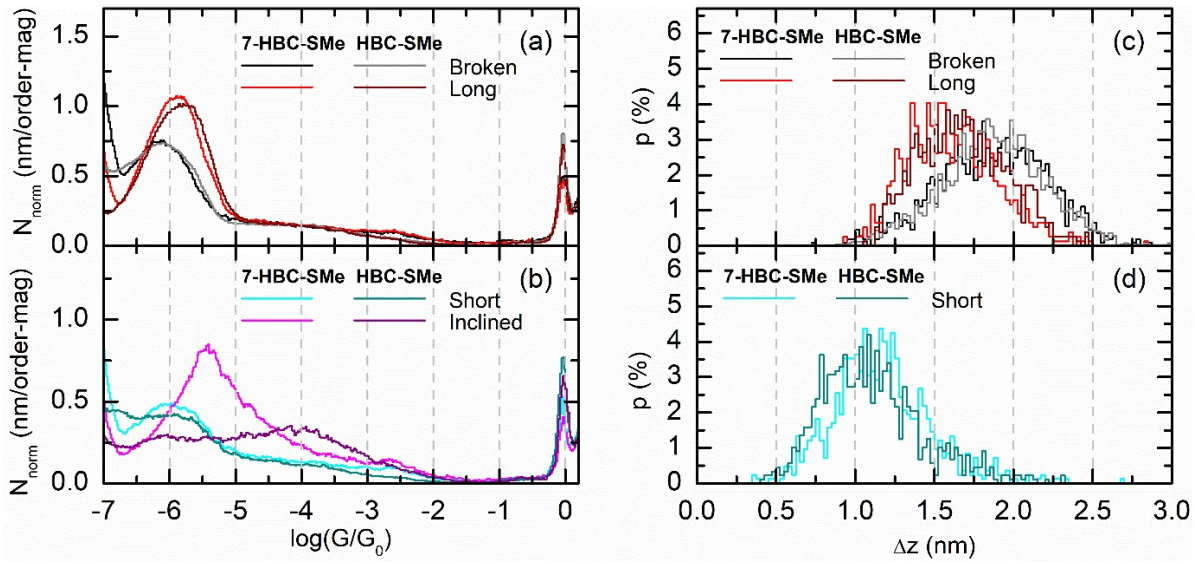

Figure S2. **a)** 1D histograms built for the different groups of *G-z* traces obtained from the clustering-based analysis for **HBC-SMe** and **7-HBC-SMe**, and **b)** their corresponding plateau-length distributions.

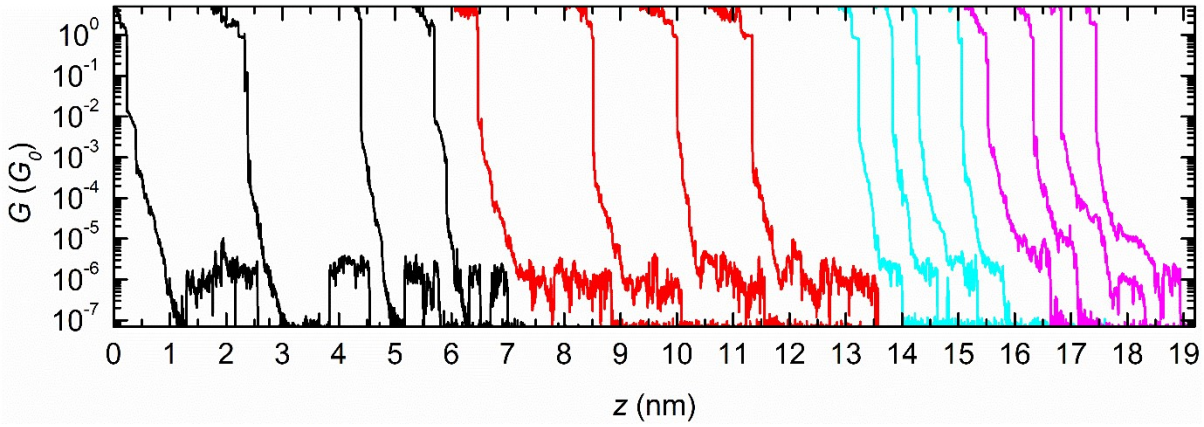

Figure S3. Individual *G-z* traces for **7-HBC-SMe**, corresponding to the four groups previously described. Black: broken plateaus; red: long plateaus; cyan: short plateaus: pink: inclined plateaus.

2.5. Comparison with 7-HPB-SMe

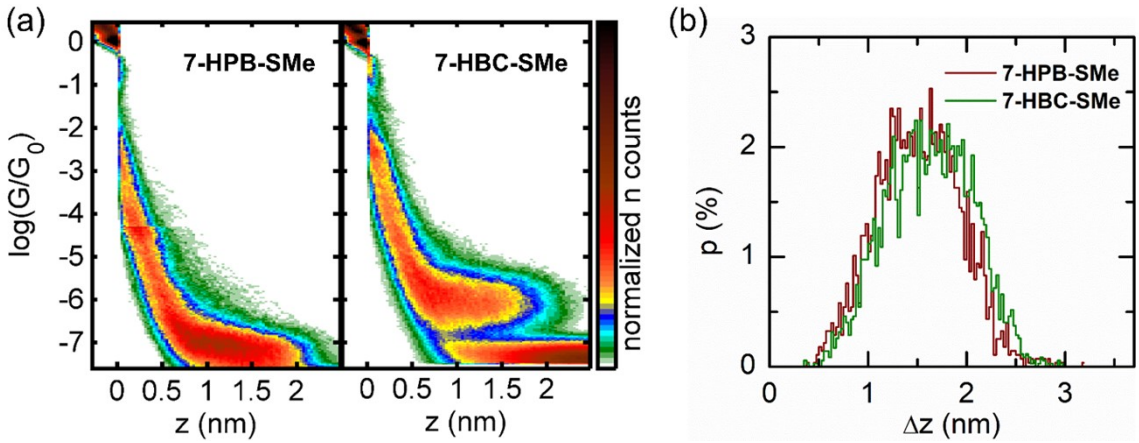

Figure S4. Results for the single-molecule experiments for **7-HPB-SMe**. a) 2D histogram of all traces displaying plateaus; b) plateau-length distribution in comparison with that of **7-HBC-SMe**.

2.6. Single-molecule conductance for 7-HBC-alk and HBC-alk:

Despite alkyne-terminated molecules have been previously used as linking groups in STM-BJ experiments, the complexity of the typically obtained 1D and 2D histograms requires a detailed analysis and discussion for ensuring a proper interpretation of results.

As mentioned in the main text, the 1D histograms reveal a multipeak signal, which normally indicates that more than one process is present in the recorder *G-z* traces. Clustering based analyses have demonstrated to be very useful in these cases, since they are able to distinguish different breaking profiles within the full set of *G-z* traces. For **7-HBC-alk** and **HBC-alk,** we distinguished up to three groups (A, B and C), which differ in both, the profile and the conductance range in which they display the molecular signal. The 2D histograms of these groups are shown in Figure 4a in the main text. Both compounds show equivalent profile and proportion for each group. As observed in the 1D histograms (Figure 4b), each group is also centered at the same conductance value for both molecules, reinforcing that both of them attend to the same electrical behavior. Small variations in the profile of the

histograms can be attributed to experimental run-to-run variations rather than to differences between both compounds, as evidenced by Figure S5 that compares histograms from different runs for **7-HBC-alk**.

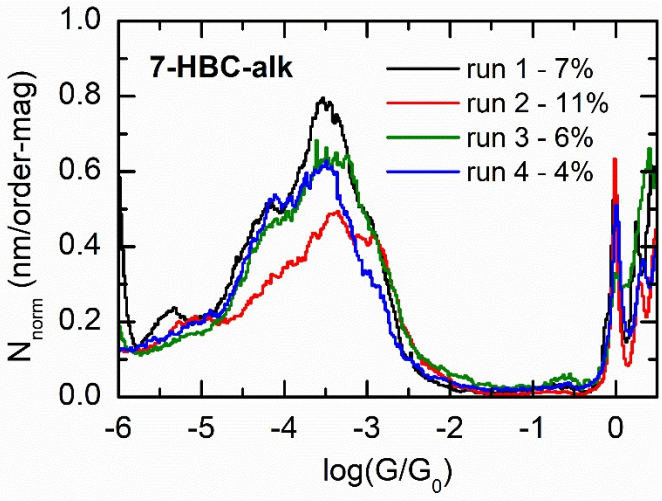

Figure S5. 1D histograms obtained for **7-HBC-alk** in 4 different experimental runs. The value indicated for each run corresponds to the percentage of traces with plateaus respect to the total number of recorded traces. The main features are reproduced in all histograms, although with different weight, reflecting different occurrence of the different possible configurations.

A striking difference between the groups is the shape of the corresponding breaking feature. Groups A and B are formed by *G-z* traces displaying a flat region followed by a bulged conductance fall, while group C is formed by sloping and inclined traces. For better illustrating this, some representative individual *G-z* traces from each group can be found in Figure S6.

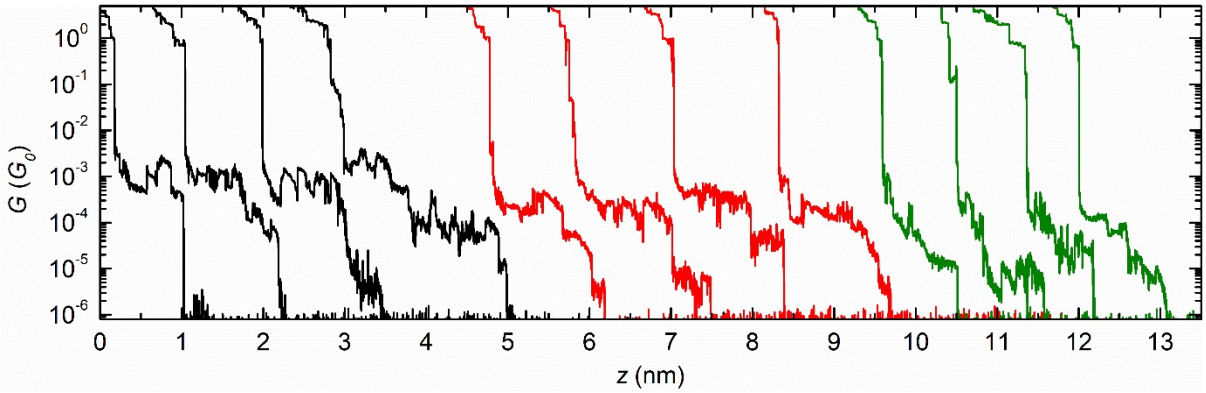

Figure S6. Individual G-z traces for **7-HBC-alk**. Four examples are shown for traces in groups A (black), B (red) and C (green) separated using a clustering-based analysis.

Groups A and B are especially relevant, since the drastic change in the trace profile along the breaking seems to indicate the transition between different processes. Thus, two different plateau-length distributions were obtained for these groups. The first one, until the end of the flat region (Figure S7-top), and the second one, until the end of the bulged tail (Figure S7-bottom). We observed that the end of the shorter distribution concurs well

with the value of the expected plateau-length for the molecule fully extended between the electrodes (marked as a dashed line), similarly as it happens for amine[7] and -SMe[8] terminated molecules. In contrast, the distribution when considering the end of the tail is shifted towards longer distances, being the end of the distribution about 0.5 nm above. This is in agreement with the theoretical work by Hoft *et al.* which tracks the evolution of the Au-diethynylbenzene-Au junction while stretching the electrodes.[9] The authors predicted a rearrangement of the gold atoms in the electrodes, due to the strong C-Au interaction, that first induces a conductance decay as separating the electrodes and secondly promotes detaching gold atoms at the breaking point. This picture is in agreement with both, the observed conductance profile in the experimental curves and the molecular junctions being stretched more than the expected length. Similar plateau-distributions have been also observed for thiol terminated compounds,[10] for which have been also suggested that Au atoms at the electrodes can be rearranged or pulled from the electrodes before the breaking of the molecule-electrode interaction.[4] Simultaneous conductance and force-microscopy experiments have demonstrated this could be possible when the energy needed for extracting adatoms from the electrodes is lower than that required for the breaking of the contact,[11] as expected for the strong C-Au interaction.

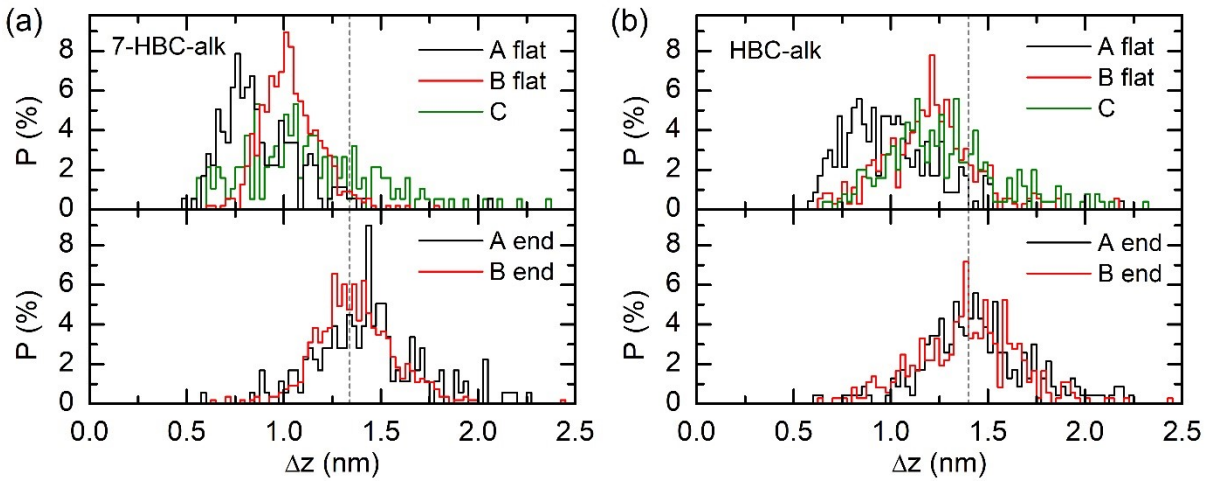

Figure S7. Plateau-length distributions for groups A, B and C and D found for **7-HBC-alk (a-c)** and **HBC-alk (d-f)**, showing separately the length at the end of the flat region and at the end of the final cloud for the groups A and B of each molecule. The length values marked as vertical lines correspond to the expected junction length for each molecule, considering the distance from the middle of the Au-C bond.

The flatter region observed in traces of groups A and B, would be then associated at a more stable junction situation, prior to the aforementioned electrode rearrangement. However, the conductance values for this flatter region in groups A and B is not exactly the same, being slightly higher in the first group. Previous studies, also observing these two flat groups of plateaus for alk-terminated molecules, have suggested the higher ones to be due to multimolecular junctions.[12] Considering the low success rate in our experiments (7% and 4% for **7-HBC-alk** and **HBC-alk,** respectively), it seems unlikely in our case. Different ways of bonding have been reported for Au and acetylene groups, involving not only σ/σ interactions, but also σ/π and π/π,[13] which would give rise to slightly different conductance values but also slightly different plateau lengths. The length distributions for groups A and B (when considering the end of the flat region) support this hypothesis. Even when concurring

at the end of the distribution, the main value of the Gaussian distribution is shifted to shorter values in group A in comparison with that of group B, indicating that they could be due to junctions involving geometries with reduced electrode-electrode separation.

I-V traces were also studied for the **7-HBC-alk/ HBC-alk** pair, revealing no appreciable difference in their behavior in the -1 V to 1 V voltage interval. They are discussed in the next section. The similarities between the two molecules are consistent with the results obtained by DFT and by tight-binding.

2.7. Current-voltage (I-V) curves

The behaviour of the *I-V* curves is generally related to the HOMO-LUMO gap: the higher the curvature of the traces, the closer in energy the HOMO or LUMO are. For these molecules, we can observe very flat curves, as shown in Figure S8 and S9, which means a big separation between the HOMO and LUMO energies. The simmetry of the curves is indicating i) that Fermi level is far away from both HOMO and LUMO, and ii) there is the same kind of molecule-electrode interation in both sides of the molecule in the junction. The latter is an additional indication of the molecules attached to the electrodes through the anchoring groups. Interestingly, for the **HBC-alk/7-HBC-alk** pair two sets of *I-V* curves can be distinguished in the 2D histograms (Figure S9), which is related to the different possible electrode-molecule interaction allowed by the terminal alkynes, and which has been dicussed in detail in the main text.

Importantly, no appreciable differences are detected between the curves from the planar and the curved molecules, in any of the studied pairs, indicating that the presence of the 7-membered ring promoting the curvature is not inducing any effect on the *I-V* characteristics.

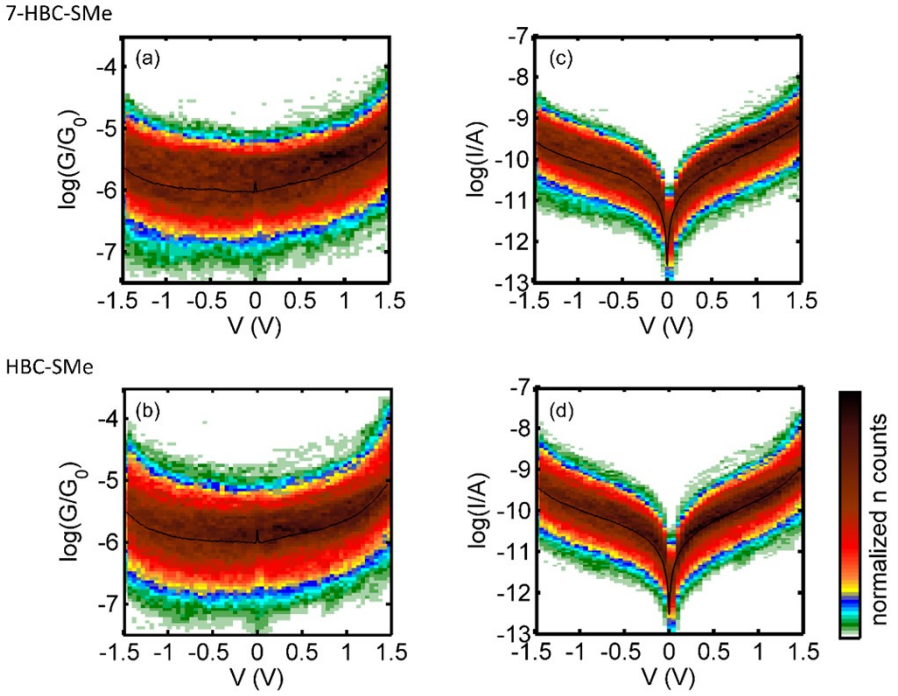

Figure S8. 2D histograms of log(G/G$_0$) *vs* V (a and c) and log(I/A) *vs* V (b and d) built from the -1.5 -1.5 voltage ramps along the molecular plateaus for **7-HBC-SMe** and **HBC-SMe**.

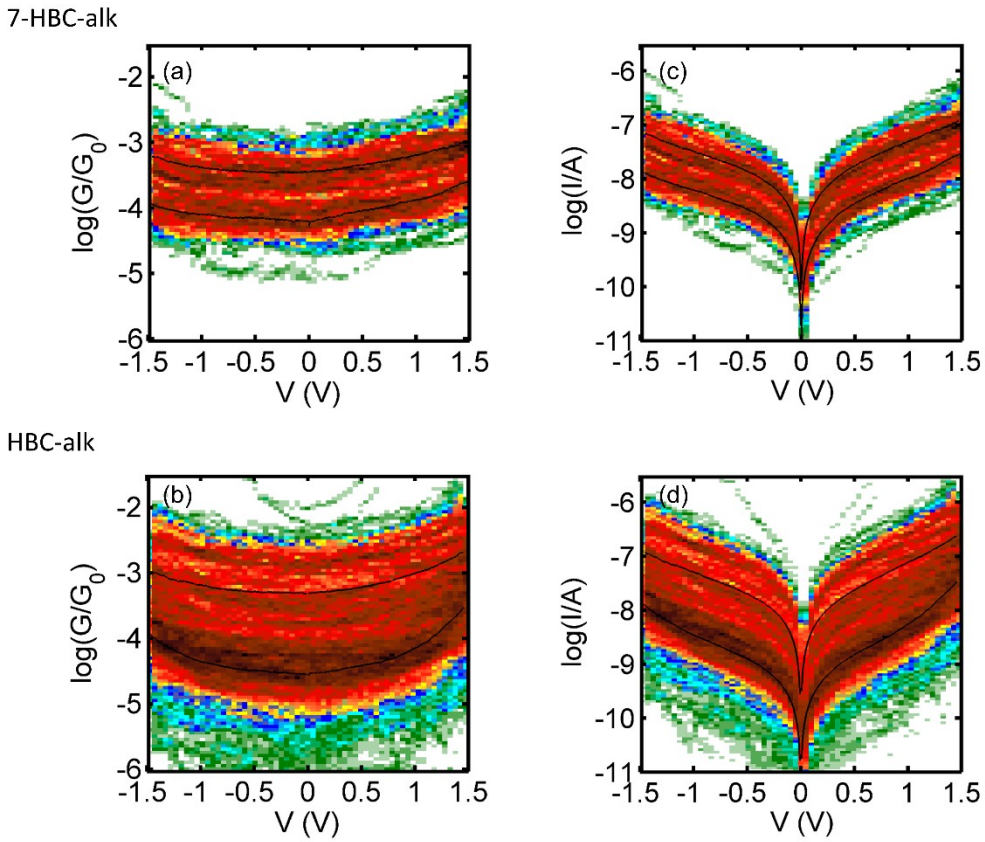

Figure S9. 2D histograms of $\log(G/G_0)$ *vs* V (a and b) and log(I/A) *vs* V built from the -1.5 - +1.5 (b and e) and -0.5 – +0.5 (c and f) voltage ramps along the molecular plateaus for **7-HBC-alk** and **HBC-alk**.

2.8 Additional comparison between the two linking groups

Besides the different breaking profile produced by the two binding groups, some other differences between them are worth mentioning. The experimental success rate (percentage of curves displaying molecular signal) could be easily modified (between 10% and 60%) for the -SMe terminated molecules, by using a solution of higher or lower concentration when preparing the samples. However, for the terminal alkynes ones, the success rate was quite low even for high concentrated solutions (between 1% and 11%, see Figure S4 in the ESI). The conductance reduction for the molecules presenting -SMe in comparison with those with terminal alkynes is in agreement with the expected conductance decay when increasing the anchor-anchor distance for the same molecular core, as also predicted by DFT and tight-binding calculations. However, the strength of the different bonding, responsible of the molecule-electrode interaction in each case, can be also contributing to the observed conductance shift.

3. Theoretical calculations

3.1. DFT-based calculations

3.1.1. Methods

Theoretical calculations based on density functional theory (DFT) and Green's function techniques were conducted to get an insight into the conductance trend observed in the experiments across the different compounds. The DFT calculations were carried out employing the code Turbomole[14] v6.4, using a BP86[15] exchange-correlation functionals and def-SVP[16] basis set. The geometrical structures of both gas-phase molecules and metal-molecule-metal junctions were optimized until the maximum norm of cartesian gradient was converged to the value of 10^{-5} and 10^{-4}, respectively. For the junctions, the optimized geometry consisted of a molecule held between two Au_{20} pyramidal clusters, in which all layers were frozen except for the four atoms closest to the molecule (i.e. at the pyramidal apex). The size of the gold clusters was then extended to 63 atoms on each side and a single-point calculation was performed on this new structure. Electron-transport calculations were then carried out in the spirit of the Landauer formalism, following the procedure described in previous works.[17] The HOMO-LUMO gap was corrected applying the DFT+sigma technique[18] as we previously described.[19]

3.1.2. Gas-phase orbitals

Figure S10 shows the spatial distribution of the HOMO for **HBC-SMe**, **7-HBC-SMe**, **HBC-alk** and **7-HBC-alk** obtained by DFT. The compounds comprising the 7-membered ring exhibit, by and large, the same HOMO structure as the planar counterparts, with some additional weight on the oxygen atom.

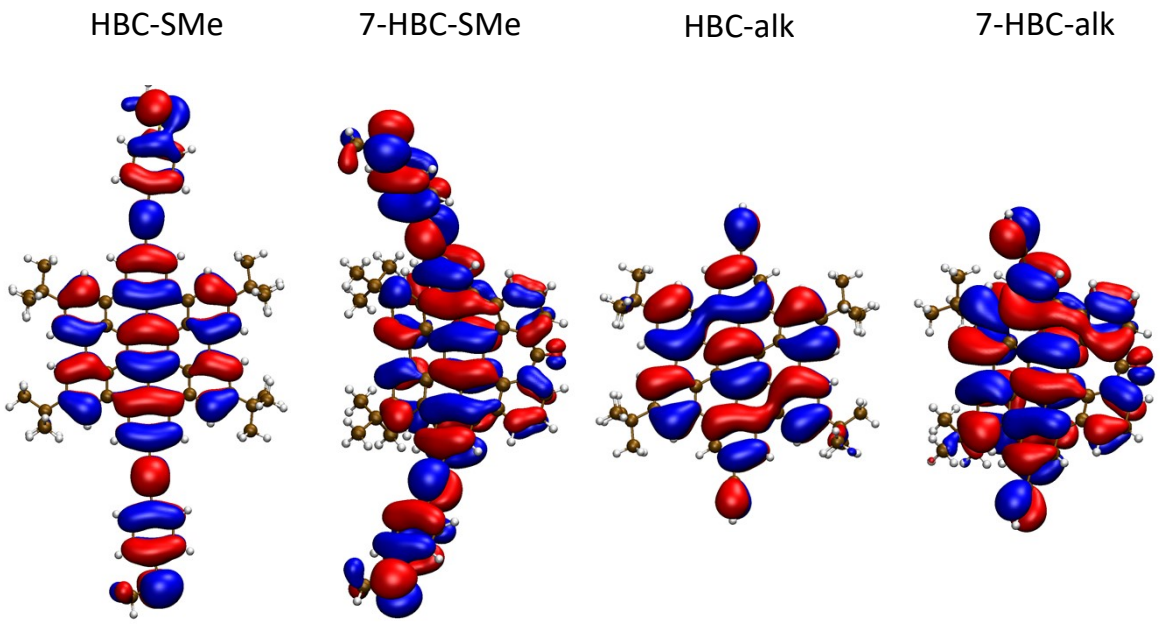

Figure S10. Visual representation of the HOMO for **HBC-SMe**, **7-HBC-SMe**, **HBC-alk** and **7-HBC-alk**.

3.1.3. Local density of states (LDOS) curves

Figure S11 shows the density of states of the junction projected on the molecules for both compounds in the top binding positions displayed in Figure 2 and 4 of the main text. The resonances closest to the Fermi level exhibit the same shifts observed in the transmission curves of the same figures, as well as the similarity of values at the Fermi level between the flat and curve compound with both anchoring groups.

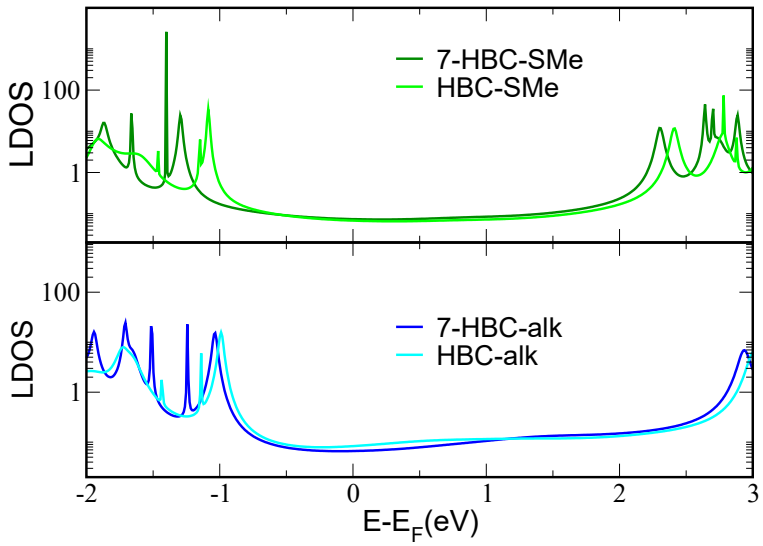

Figure S11. Local density of states (LDOS) projected on the molecule for 7-**HBC-SMe, HBC-SMe, 7-HBC-alk** and **HBC-alk** in the top binding position.

3.1.4. Transmission coefficients

The figure below shows, in addition to the total transmission already shown in Figure 2 and 4 of the main text, the transmission of the first channel (T_1), which reproduces the total transmission. This indicates that the transmission in the region around the Fermi level is dominated by a single channel. The and dotted dashed curves correspond to channels with lower contributions.

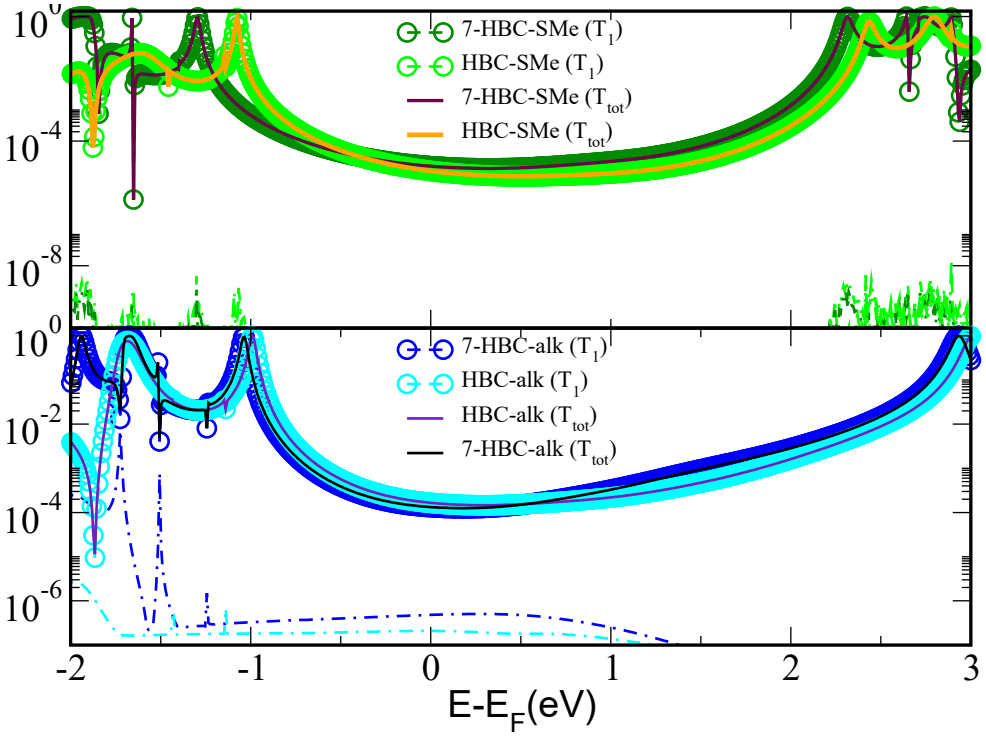

Figure S12. Total transmission (T_{tot}) and transmission of the most dominant channel (T_1) for 7-**HBC-SMe, HBC-SMe, 7-HBC-alk** and **HBC-alk** in the top binding position. The dashed-point curves are relative to lower-contribution channels.

3.2. Tight-binding calculations

Figure S13(b-c) shows the transmission curves obtained for **7-HBC** and **HBC** molecules *via* a tight-binding (TB) approach. The couplings were calculated based on the gas-phase DFT-optimized distances as previously described,[20] following the approach based on bond overlap integrals as described by Mulliken *et al*.[21] The on-site energies used (ε_O = –2.9 eV, ε_S = –3.2 eV, ε_C = 0 eV) were based on the parametrization introduced by Van-Catledge.[22] With both anchoring groups, **7-HBC** and **HBC** are found to lead to very similar values of the transmission at the Fermi level. A slight energy shift of the HOMO resonance is observed for **HBC** with respect to **7-HBC**, reflecting what is observed in the gas phase.

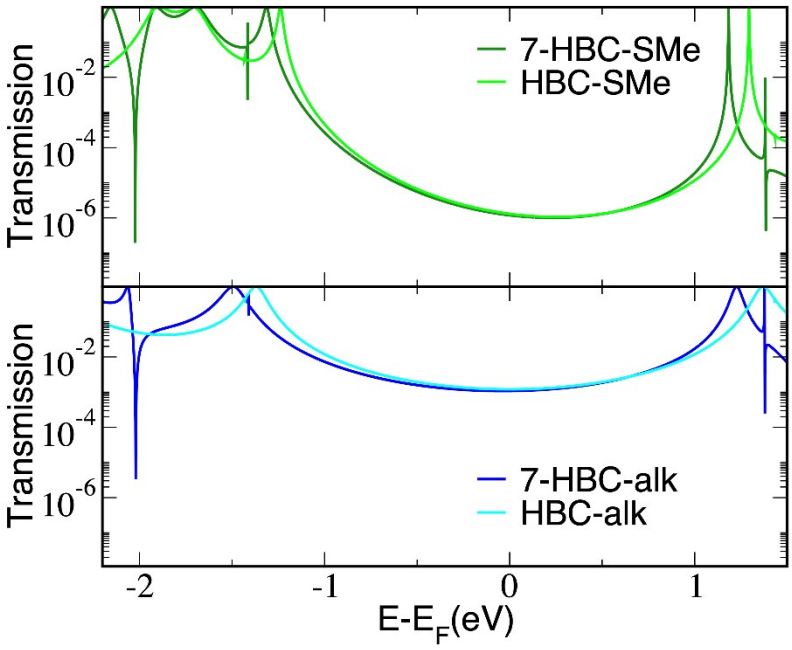

Figure S13. Transmission curves obtained by the TB approach for the **7-HBC** and **HBC** compounds ending with SMe (top) and alkyne (bottom) groups.

Table S2 reports the coupling values employed for all bonds, with the bond numbering assigned as in Figure S14. For the coupling to the leads, the values 0.5 and 1.0 eV were employed to the SMe and alkyne junctions, respectively.

Table S2. Coupling values employed, for the bonds indicated in figure S14 in the tight-binding calculations.

7-HBC-SMe

Bond	Distance	Coupling
S1-C2	1.773	1.568
C2-C3	1.418	2.958
C2-C4	1.414	2.981
C3-C5	1.395	3.078
C4-C6	1.4	3.050
C5-C7	1.424	2.931
C6-C7	1.42	2.952
C7-C8	1.424	2.932
C8-C9	1.234	3.999
C9-C10	1.425	2.926
C10-C11	1.414	2.979
C10-C12	1.415	2.972
C11-C14	1.407	3.014
C12-C16	1.405	3.024
C13-C17	1.394	3.084
C13-C18	1.417	2.966
C14-C18	1.464	2.734
C14-C21	1.428	2.910
C15-C19	1.41	2.998
C15-C20	1.407	3.016
C16-C20	1.466	2.729
C16-C21	1.435	2.874
C17-C22	1.398	3.062
C18-C23	1.442	2.843
C19-C24	1.405	3.026
C20-C26	1.428	2.912
C21-C25	1.449	2.808
C22-C27	1.408	3.012
C23-C27	1.428	2.911
C23-C28	1.481	2.658
C24-C29	1.415	2.977
C25-C28	1.443	2.838
C25-C30	1.432	2.889
C26-C29	1.43	2.899
C26-C30	1.446	2.820
C27-C31	1.488	2.624
C28-C34	1.453	2.790
C29-C35	1.466	2.725
C30-C33	1.416	2.970
C31-O32	1.229	4.029
C31-C36	1.488	2.624
C33-C37	1.432	2.889
C33-C38	1.446	2.820
C34-C37	1.443	2.838
C34-C40	1.481	2.658
C35-C38	1.43	2.899
C35-C39	1.415	2.977
C36-C40	1.428	2.911
C36-C41	1.408	3.012
C37-C42	1.449	2.808
C38-C43	1.428	2.912
C39-C45	1.405	3.026
C40-C44	1.442	2.843
C41-C46	1.398	3.062
C42-C47	1.428	2.910
C42-C48	1.435	2.874
C43-C48	1.466	2.729
C43-C49	1.407	3.016
C44-C47	1.464	2.734
C44-C50	1.417	2.966
C45-C49	1.41	2.998
C46-C50	1.394	3.084
C47-C51	1.407	3.014
C48-C52	1.405	3.024
C51-C53	1.414	2.979
C52-C53	1.415	2.972
C53-C54	1.425	2.926
C54-C55	1.234	3.999
C55-C56	1.424	2.932
C56-C57	1.42	2.952
C56-C58	1.424	2.931
C57-C59	1.4	3.051
C58-C60	1.395	3.078
C59-C61	1.414	2.981
C60-C61	1.418	2.958
C61-S62	1.773	1.568

HBC-SMe

Bond	Distance	Coupling
C1-C2	1.42	2.952
C1-C6	1.4	3.050
C2-C3	1.424	2.932
C2-C7	1.424	2.930
C3-C4	1.395	3.077
C4-C5	1.418	2.959
C5-C6	1.414	2.982
C5-S60	1.773	1.567
C7-C8	1.234	4.000
C8-C9	1.426	2.922
C9-C10	1.412	2.989
C9-C14	1.413	2.987
C10-C11	1.407	3.014
C11-C12	1.437	2.866
C11-C18	1.469	2.714
C12-C13	1.437	2.867
C12-C15	1.447	2.815
C13-C14	1.407	3.017
C13-C21	1.47	2.709
C15-C16	1.432	2.888
C15-C19	1.433	2.886
C16-C17	1.449	2.808
C16-C30	1.431	2.896
C17-C18	1.431	2.897
C17-C43	1.434	2.881
C18-C48	1.413	2.983
C19-C20	1.449	2.809
C19-C28	1.43	2.898
C20-C21	1.433	2.884
C20-C22	1.431	2.893
C21-C25	1.409	3.005
C22-C23	1.413	2.983
C22-C26	1.468	2.716
C23-C24	1.403	3.037
C24-C25	1.407	3.016
C26-C27	1.434	2.879
C26-C34	1.41	3.002
C27-C28	1.448	2.811
C27-C31	1.431	2.896
C28-C29	1.433	2.885
C29-C30	1.432	2.888
C29-C36	1.447	2.818
C30-C37	1.449	2.809
C31-C32	1.413	2.985
C31-C35	1.469	2.713
C32-C33	1.403	3.036
C33-C34	1.407	3.017
C35-C36	1.437	2.866
C35-C42	1.407	3.015
C36-C39	1.437	2.866
C37-C38	1.431	2.897
C37-C44	1.434	2.882
C38-C39	1.469	2.714
C38-C47	1.413	2.984
C39-C40	1.407	3.015
C40-C41	1.412	2.988
C41-C42	1.412	2.988
C41-C51	1.426	2.922
C43-C44	1.469	2.711
C43-C50	1.409	3.005
C44-C45	1.409	3.005
C45-C46	1.407	3.015
C46-C47	1.403	3.037
C48-C49	1.403	3.037
C49-C50	1.407	3.015
C51-C52	1.234	4.000
C52-C53	1.424	2.930
C53-C54	1.424	2.932
C53-C58	1.42	2.952
C54-C55	1.395	3.077
C55-C56	1.418	2.959
C56-C57	1.414	2.982
C56-S59	1.773	1.566
C57-C58	1.4	3.050

7-HBC-alk

Bond	Distance	Coupling
C1-C2	1.428	2.912
C1-C7	1.488	2.625
C1-C12	1.407	3.013
C2-C3	1.481	2.657
C2-C15	1.441	2.844
C3-C4	1.453	2.789
C3-C16	1.443	2.837
C4-C5	1.481	2.657
C4-C19	1.443	2.837
C5-C6	1.428	2.911
C5-C8	1.441	2.845
C6-C7	1.488	2.625
C6-C11	1.407	3.013
C7-O44	1.229	4.031
C8-C9	1.417	2.965
C8-C37	1.464	2.736
C9-C10	1.393	3.085
C10-C11	1.398	3.062
C12-C13	1.398	3.061
C13-C14	1.393	3.085
C14-C15	1.417	2.965
C15-C30	1.464	2.736
C16-C17	1.432	2.890
C16-C27	1.45	2.804
C17-C18	1.417	2.965
C17-C24	1.447	2.819
C18-C19	1.432	2.891
C18-C20	1.447	2.816
C19-C23	1.45	2.801
C20-C21	1.427	2.912
C20-C26	1.43	2.901
C21-C22	1.465	2.732
C21-C43	1.407	3.014
C22-C23	1.435	2.877
C22-C34	1.406	3.018
C23-C37	1.428	2.911
C24-C25	1.433	2.887
C24-C29	1.425	2.924
C25-C26	1.467	2.721
C25-C40	1.41	2.999
C26-C41	1.414	2.980
C27-C28	1.435	2.875
C27-C30	1.428	2.910
C28-C29	1.464	2.736
C28-C33	1.407	3.016
C29-C38	1.411	2.994
C30-C31	1.408	3.009
C31-C32	1.411	2.993
C32-C33	1.412	2.990
C32-C46	1.432	2.892
C34-C35	1.412	2.988
C35-C36	1.411	2.994
C35-C45	1.432	2.892
C36-C37	1.408	3.008
C38-C39	1.406	3.020
C39-C40	1.409	3.005
C41-C42	1.405	3.025
C42-C43	1.41	3.001
C45-C47	1.226	4.050
C46-C48	1.226	4.050

HBC-alk

Bond	Distance	Coupling
C1-C2	1.432	2.889
C1-C6	1.431	2.894
C1-C8	1.449	2.808
C2-C3	1.433	2.887
C2-C9	1.448	2.811
C3-C4	1.431	2.896
C3-C10	1.449	2.809
C4-C5	1.433	2.886
C4-C11	1.448	2.811
C5-C6	1.432	2.890
C5-C12	1.448	2.814
C6-C7	1.449	2.809
C7-C13	1.431	2.897
C7-C17	1.434	2.881
C8-C18	1.434	2.881
C8-C22	1.431	2.897
C9-C38	1.436	2.868
C9-C42	1.436	2.869
C10-C33	1.433	2.884
C10-C37	1.431	2.894
C11-C28	1.434	2.880
C11-C32	1.431	2.897
C12-C23	1.437	2.868
C12-C27	1.437	2.868
C13-C14	1.413	2.983
C13-C27	1.468	2.716
C14-C15	1.403	3.038
C15-C16	1.407	3.015
C16-C17	1.409	3.005
C17-C18	1.469	2.711
C18-C19	1.409	3.005
C19-C20	1.407	3.015
C20-C21	1.403	3.038
C21-C22	1.413	2.983
C22-C38	1.468	2.716
C23-C24	1.408	3.010
C23-C32	1.468	2.716
C24-C25	1.41	3.001
C25-C26	1.41	3.002
C25-C44	1.432	2.889
C26-C27	1.408	3.010
C28-C29	1.41	3.002
C28-C37	1.468	2.716
C29-C30	1.407	3.017
C30-C31	1.403	3.036
C31-C32	1.413	2.985
C33-C34	1.409	3.005
C33-C42	1.469	2.711
C34-C35	1.407	3.016
C35-C36	1.403	3.036
C36-C37	1.413	2.983
C38-C39	1.408	3.009
C39-C40	1.409	3.003
C40-C41	1.41	3.001
C40-C43	1.432	2.889
C41-C42	1.408	3.012
C43-C45	1.226	4.049
C44-C46	1.226	4.049

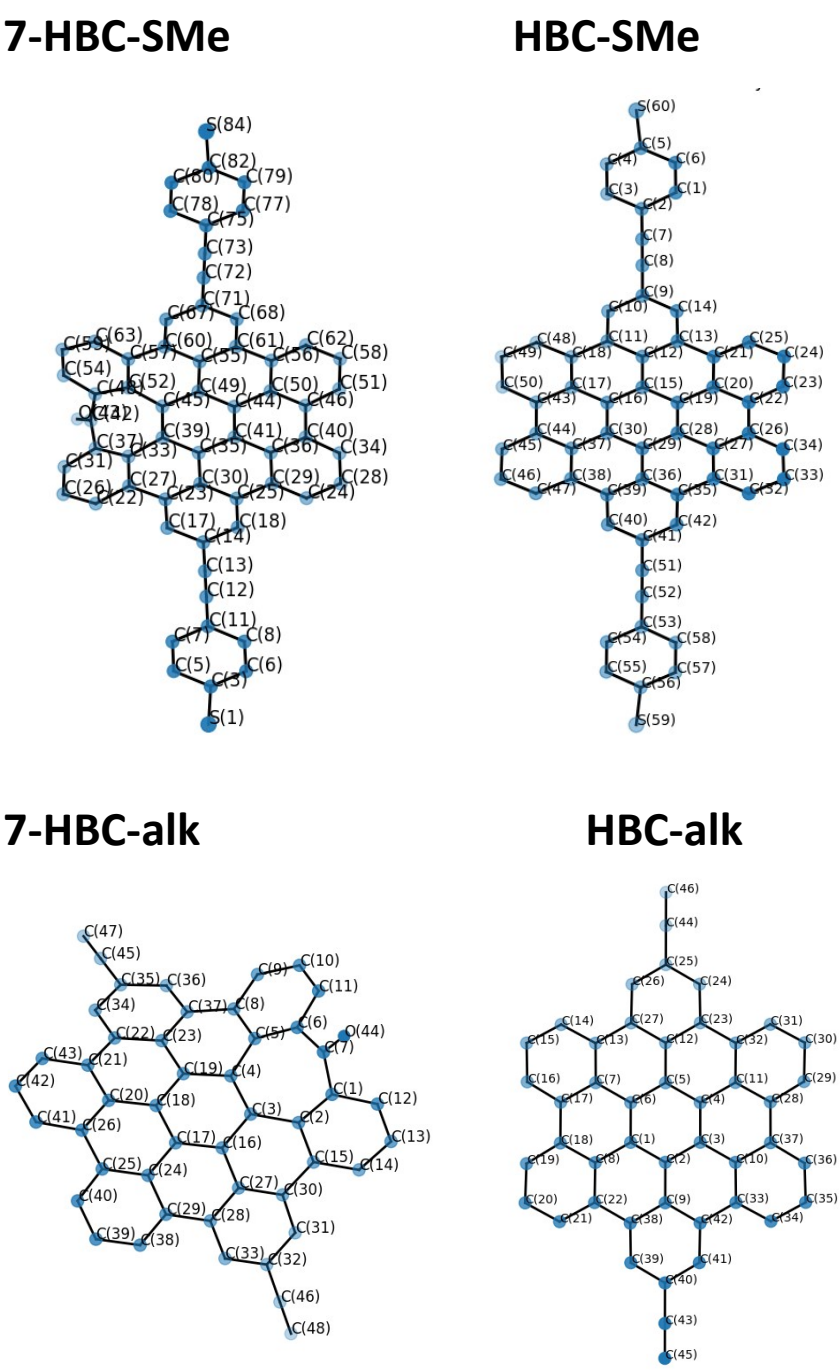

Figure S14. Assignment of the atom indexes corresponding to the coupling values listed in table S2.

3.3. Additional DFT-based calculations.

3.3.1. Comparison with 7-HPB-SMe and other molecules

In the figure below (S15), we compare the transmission curves of **7-HBC-SMe** and **HBC-SMe** (reported in the main text) with those obtained, in similar top binding geometries, for the following compounds: **7-HPB-SMe** (scheme S4); **Terphen-SMe**, which was obtained by first extracting the central backbone of the HBC junction, and by then reoptimizing the

geometrical structure while keeping the same Au-Au-distance; **OPE3-SMe**.[8] The computed conductance values for **7-HPB-SMe**, **Terphen-SMe** and **OPE3-SMe** are found to be 9.8 x $10^{-7}G_0$, 5.7 x $10^{-6}G_0$ and 1.3 x $10^{-4}G_0$, respectively. The lower degree of conjugation in **7-HPB-SMe** compared to **7-HBC-SMe** causes a decrease in the conductance, the common logarithm of their ratio (1.2) being in excellent agreement with that found experimentally (see Figure S4). We also observe that replacing the π-extended core (HBC or 7-HBC) with a benzene ring as in **OPE3-SMe** leads to a conductance increase, in agreement with previous experimental observations. **Terphen-SMe** (not measured experimentally), however, offers further insight into the role of conjugation, as we proceed to explain. Given that the electrical conductance in byphenyl junctions was shown to be proportional to the cosine squared of the torsion angle φ,[23] for a system with three consecutive rings the same is expected to be proportional to the fourth power of this angle. Considering the different average torsion angles between the three rings of the central backbone (0° for **HBC-SMe**, ~36° for **Terphen-SMe**, and ~63° for **7-HPB-SMe**), it can be observed that, as a rule of thumb, the ratios between the theoretical conductance values of these three compounds indeed fit well with the ratios expected from the $\cos^4\varphi$ rule. All in all, these results show that differences in the torsion angle of the molecular backbone have larger impact on the conductance that the induced curvature here for HBC cores does.

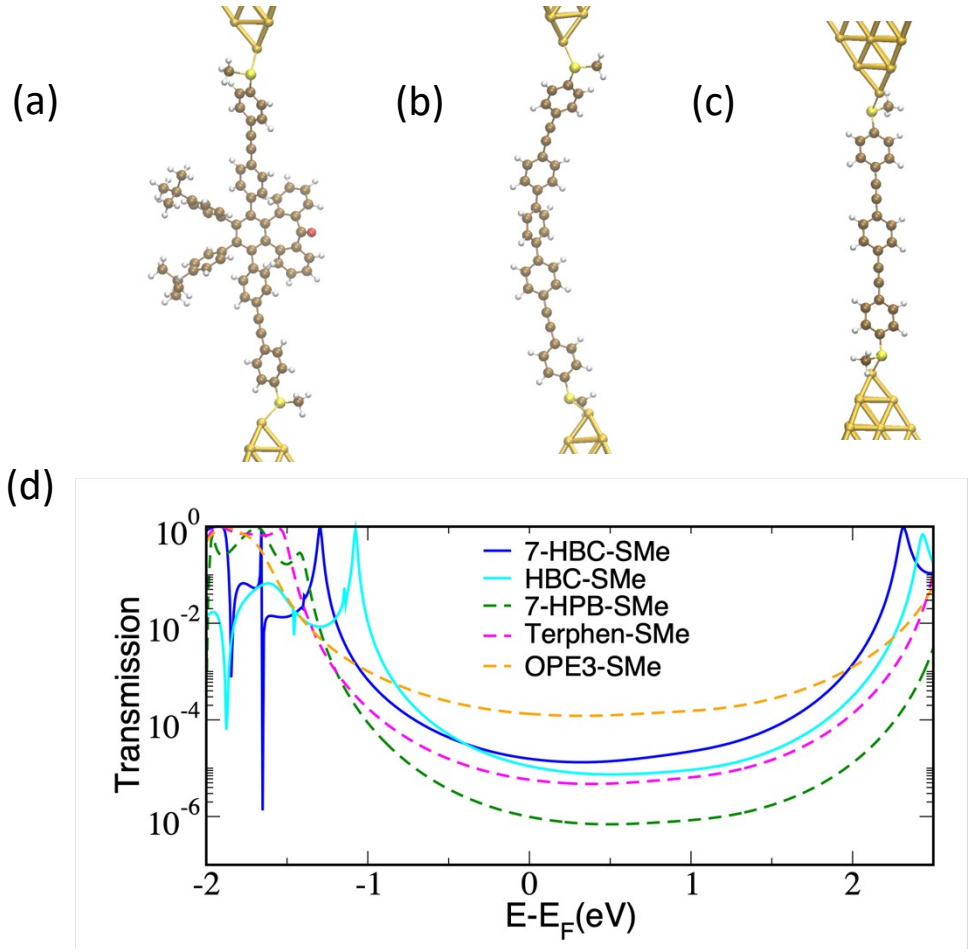

Figure S15. Molecular junctions comprising **7-HPB-SMe** (a), **Terphen-SMe** (b) and **OPE3-SMe** (c), and corresponding transmission curves (d), compared with those of **7-HBC-SMe** and **HBC-SMe** already shown in the main text.

3.3.2. HBC-alk and 7-HBC-alk in the bridge position.

Figure S16 shows a comparison between the transmission curves obtained for **HBC-alk** and **7-HBC-alk** in the bridge position with those obtained in the top position (which were already shown in Figure 4 of the main text). For both compounds, the bridge position shifts the HOMO resonance to lower energies. However, this is counteracted by the higher broadening of the peak, resulting in higher conductance than in the top position.
We also observe that, in both configurations, the two compounds show similar conductance, showing once again a minimal impact of the curvature on the transport properties.

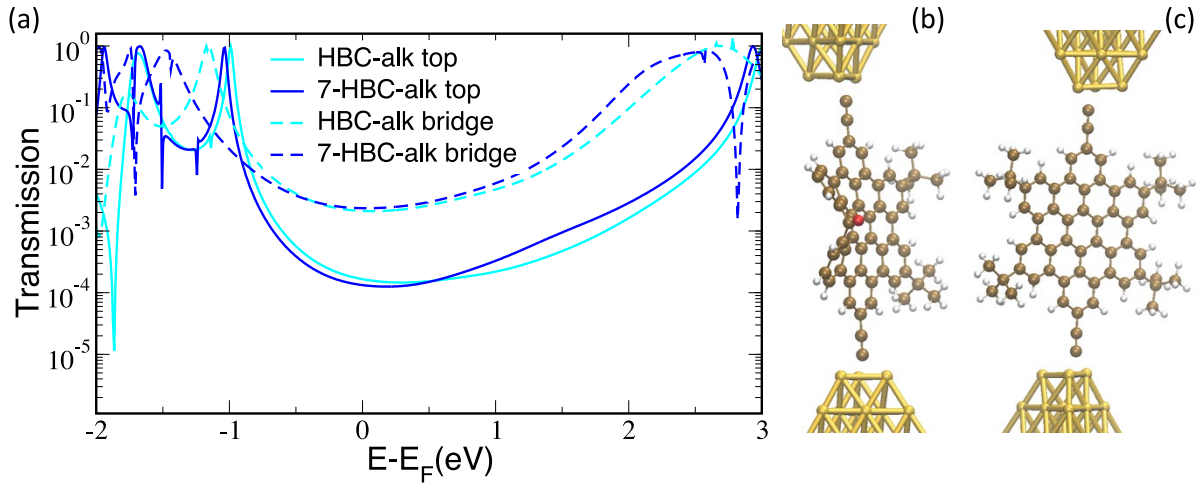

Figure S16: Transmission curves (a) for **HBC-alk** (cyano) and **7-HBC-alk** (blue) in the top (solid line) and bridge (dashed line). **7-HBC-alk** (b) and **HBC-alk** (c) in the bridge binding positions corresponding to the curves shown in panel a.

3.3.3. The role of curvature vs chemical functionalization

In order to understand the slightly unexpected result that the curved **7-HBC** compound displays a lower lying HOMO compared to the flat HBC, we decided to analyze the gas-phase energies of two analogous compounds (Table S3).
As it is known that CO is typically an electron withdrawing group, we decided to analyze the gas-phase energetics by replacing, in **7-HBC-alk**, the CO group with CH_2 and NCH_3. These groups preserve the overall curvature but should act as mild to moderate electron donating groups instead (see the figure below for a comparison between the charge-density distribution in the CO and CH_2-substituted compounds). Substitution with CH_2 and NCH_3 gave rise to HOMO energies 0.21 and 0.46 eV higher than in **7-HBC-alk**, respectively. This is consistent with their electron donating character.
Notably, however, the HOMO position of the CH_2-functionalized compound is almost identical to that of the flat **HBC-alk**. The CH_2-functionalized compound can be regarded as the closest possible "curved" version of the flat HBC-alk, since insertion of CH_2 into the flat structure is the minimum chemical modification conceivable to achieve the desired curvature. Having removed the electron-withdrawing effect of the CO group, one might then expect the curvature in the CH_2 compound to raise the HOMO energy with respect to the flat HBC-alk (according to the sign distribution of the HOMO wavefunction, in line with

what discussed in Ref. 47 of the main text). The fact that, instead, the HOMO of these two compounds has practically the same energy suggests that there is something else at play, which prevents the curvature from positioning the HOMO of the CH_2-functionalized compounds above that of the flat HBC-alk. The most obvious reason for this can be put down to the simultaneous break in conjugation between adjacent phenyl rings caused by insertion of the additional C needed for the heptagonal ring. Such a break happens irrespective of, the chosen group (CO, CH_2 and NCH_3), which will tend to widen the HOMO-LUMO gap. All in all, this indicates that the lower energetic alignment of the HOMO in **7-HBC-alk** with respect to the HOMO of **HBC-alk** is determined by the combination of two effects which both shift it to lower energies: the electron-withdrawing effect of the CO group on the one hand, and the break in the conjugation (also induced by the presence of CO) on the other.

Table S3. HOMO and LUMO values obtained by gas-phase DFT calculations for the alk-pair and two additional 7-HBC variants with CH_2 and NCH_3 instead of CO in the 7-membered ring.

	HOMO (eV)	**LUMO (eV)**
HBC-alk	–4.99	–2.68
7-HBC-alk	–5.21	–2.90
CH_2 7-HBC-alk	–5.00	–2.69
NCH_3 7-HBC-alk	–4.75	–2.65

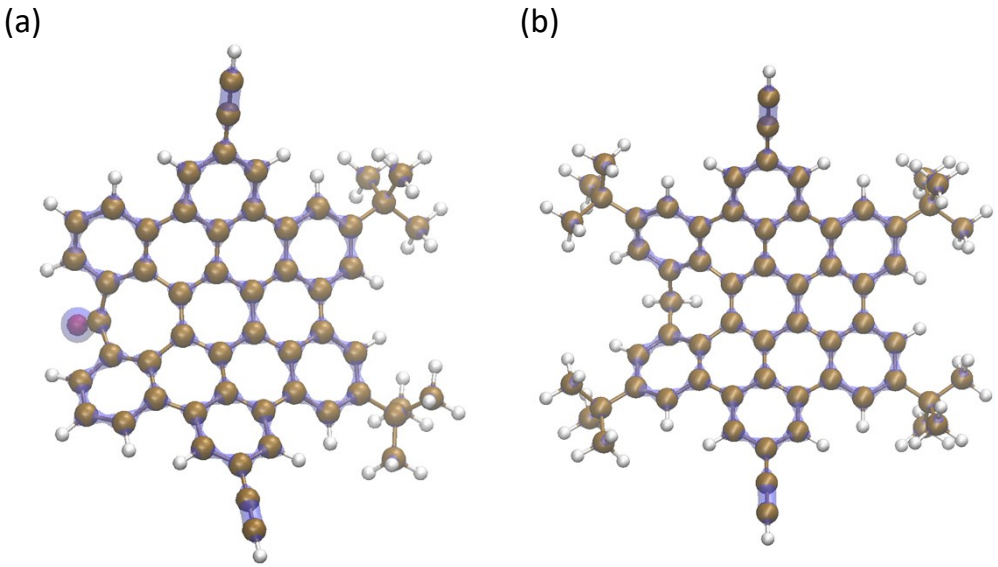

Figure S17: Electron density for **7-HBC-alk** and **CH_2 7-HBC-alk**. The CO group in **7-HBC-alk** is electron-withdrawing, attracting charge density, whereas the CH2 is donating, thus surrounded by less charge density than the rest of the molecules.

4. Self-assembled monolayers (SAMs) preparation and characterization.

4.1 SAMs preparation

All SAMs were prepared on template stripped gold surfaces.[24] In the case of **HBC-alk** and **7-HBC-alk** the freshly prepared substrates were immersed in a 0.4 mM solution in chlorobenzene for 20 hours, under argon atmosphere and light exclusion. After the incubation time, the substrates were vigorously rinsed with chlorobenzene and dried under N_2 stream. In the case of the **HBC-SMe** and **7-HBC-SMe**, the same protocol was followed but using a 0.01mM solution of the molecules.

4.2 Cyclic voltammetry characterization

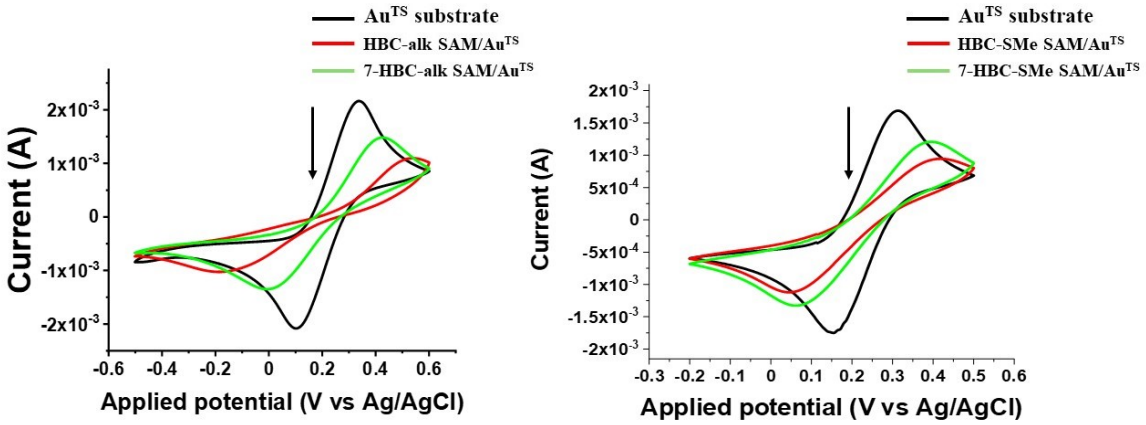

Figure S18. Electrochemical experiments using a solution of 0.1 M KCl as electrolyte in Milli-Q water with 0.01 M of $[Fe(CN)_6]^{3-/4-}$ as redox marker. Bare Au and functionalized substrates were used as working electrode, a Pt wire as counter electrode and an Ag/AgCl electrode as reference. CV recorded at 0.1 $V \cdot s^{-1}$ scan rate.

Cyclic voltammetry analysis was performed in a custom-built glass electrochemical cell using an AUTOLAB 204 Potentiostat with NOVA 2.1.6 software. To qualitatively evaluate the surface coverage of the monolayers, cyclic voltammetry experiments were carried out using the $[Fe(CN)_6]^{3-/4-}$ as redox probe in solution (Figure S18).

4.3 Charge transport measurements across HBC monolayers using the "EGaIn technique"

Charge transport measurements across the junctions with the configuration: EGaIn/GaOx/SAMs/Au^{TS} were performed in a home-built set-up. To prepare the top contact, the EGaIn electrode was shaped as a cone following previously reported methodologies.[25] In this work, the tip diameter that was brought into contact with the sample surfaces was around 25 µm.[26] The bottom electrode was grounded. The top electrode was biased from 0V →0.5V→ 0V → -0.5 V→ 0V. For each sample, 20 traces on 30 junctions were collected, with a step size of 50 mV, integration time of 100 ms, and a delay of 50 ms, for acquiring the J(V) curves. The tip was renewed every three junctions. Yield of junction formation = 90% for **HBC-alk** and 7-**HBC-alk** SAMs and 57% for **HBC-SMe** and **7-HBC-SMe** SAMs.

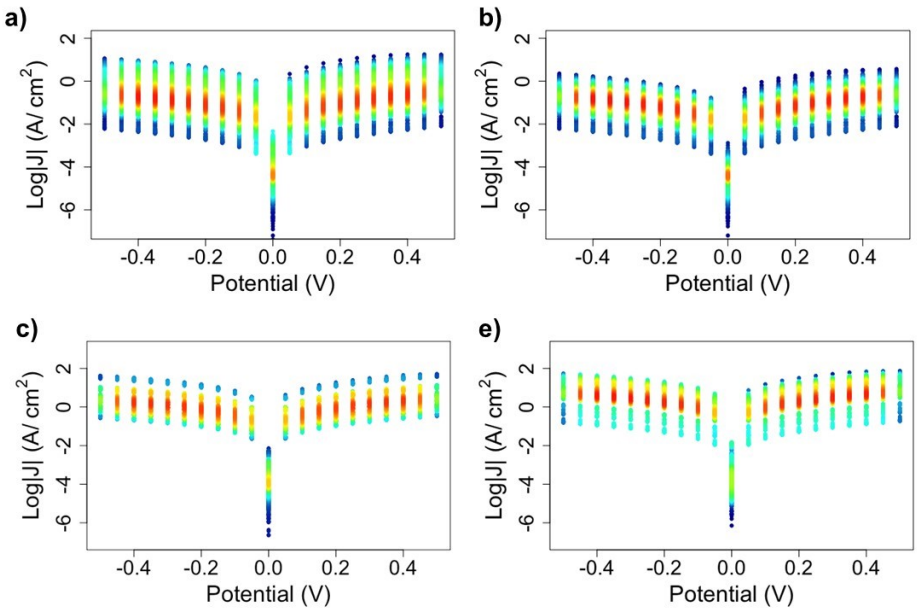

Figure S19. JV characteristics (heat map plots) of the EGaIn/GaOx/SAMs/Au^{TS} for a) **HBC-alk**, b) **7-HBC-alk**, c) **HBC-SMe** and d) **7-HBC-SMe** SAMs.

5. NMR spectra

7-HBC-SMe

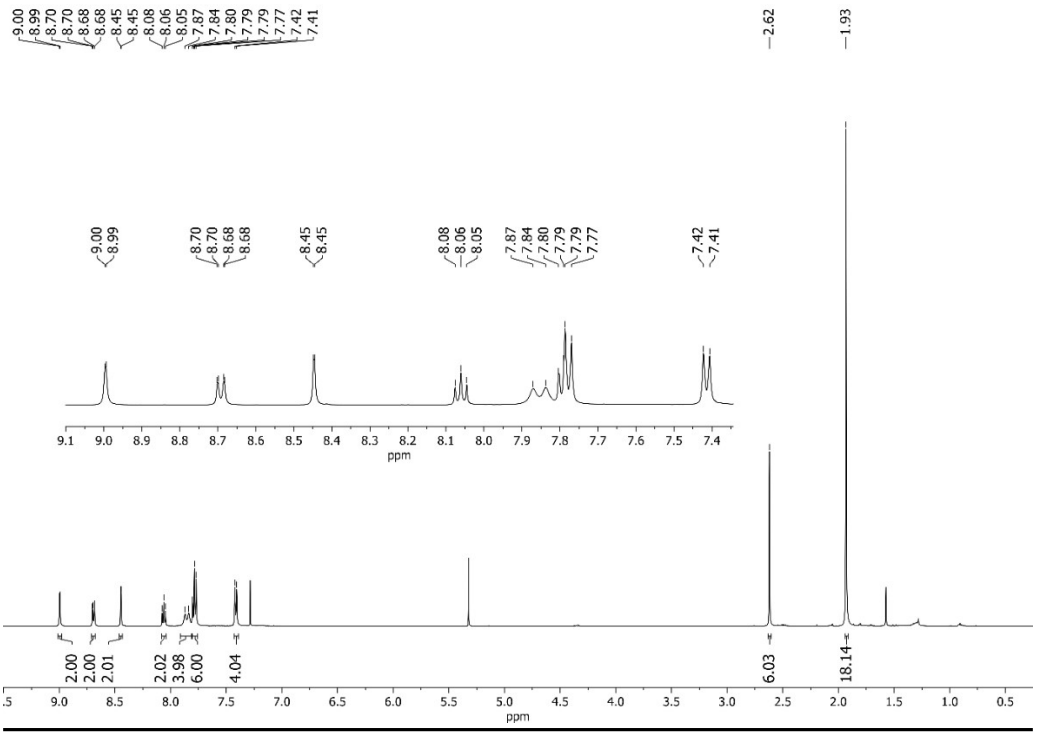

Figure S20. ^{1}H NMR (500MHz, $CDCl_3$) spectrum of compound **7-HBC-SMe**. Inset: zoom in the aromatic region.

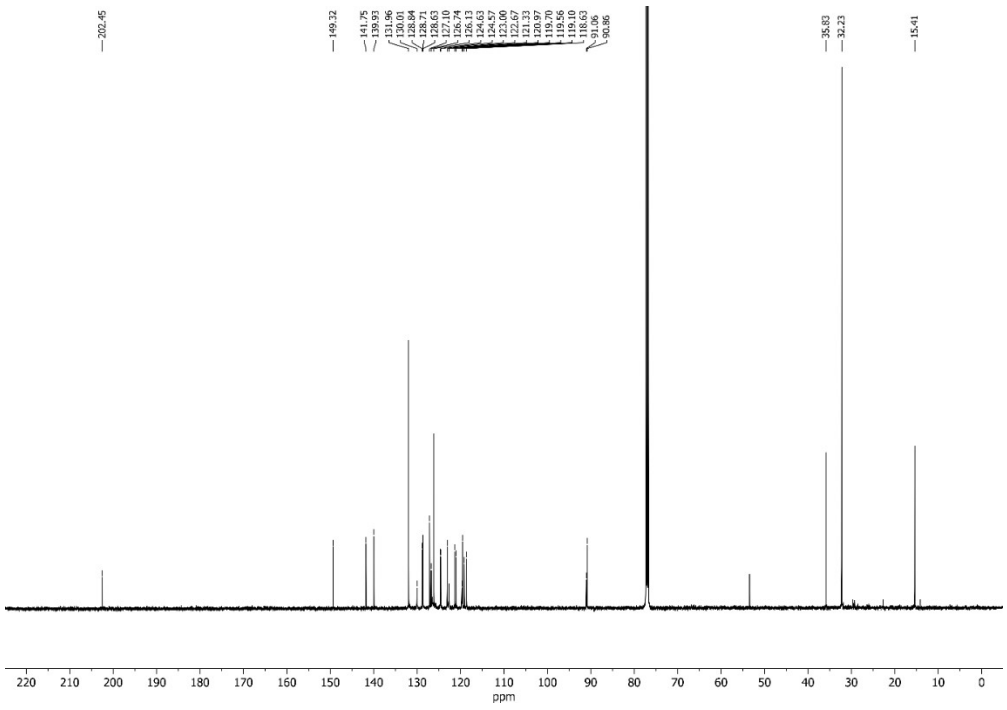

Figure S21. ^{13}C NMR (126 MHz, $CDCl_3$) spectrum of compound **7-HBC-SMe**.

7-HBC-alk

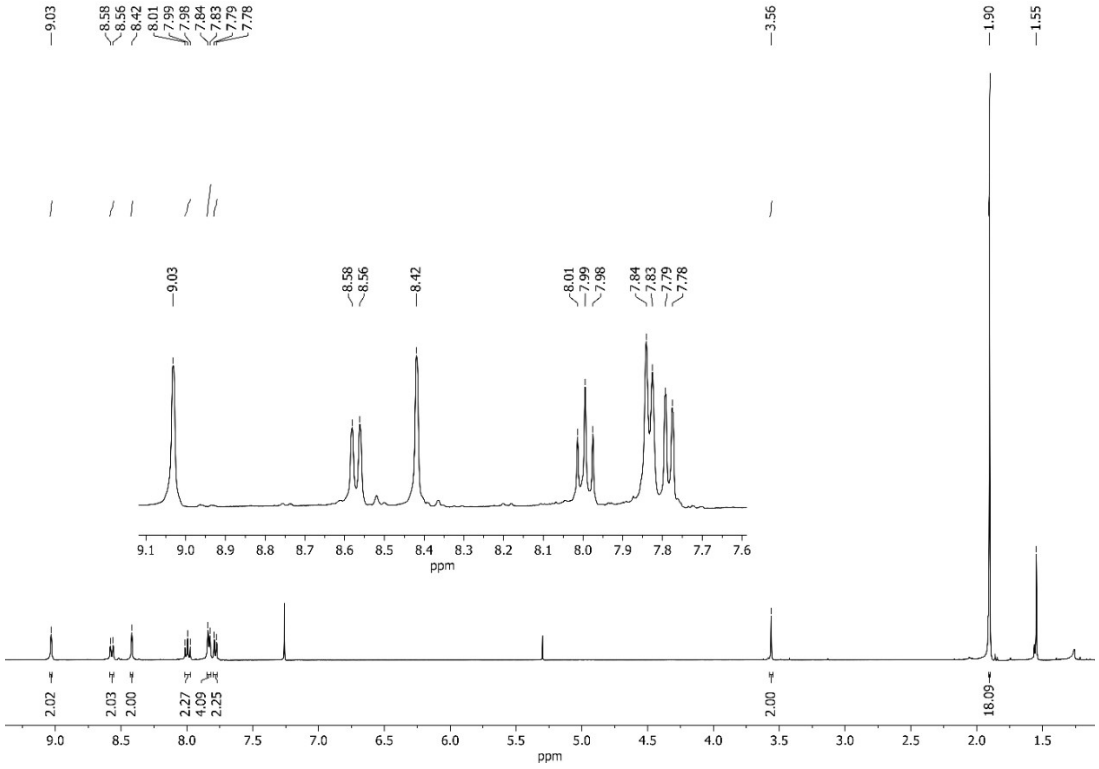

Figure S22. ^{1}H NMR (500MHz, $CDCl_3$) spectrum of compound **7-HBC-alk.** Inset: zoom in the aromatic region.

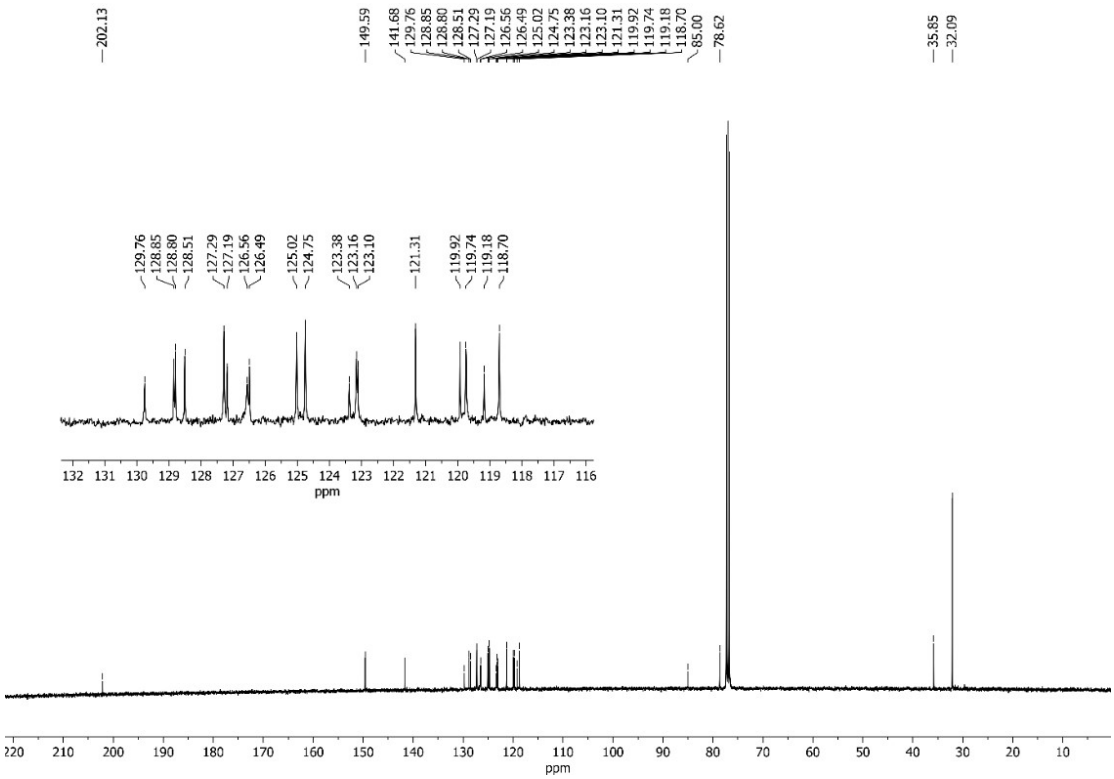

Figure S23. ^{13}C NMR (126 MHz, $CDCl_3$) spectrum of compound **7-HBC-alk.** Inset: zoom in the aromatic region.

HBC-alk:

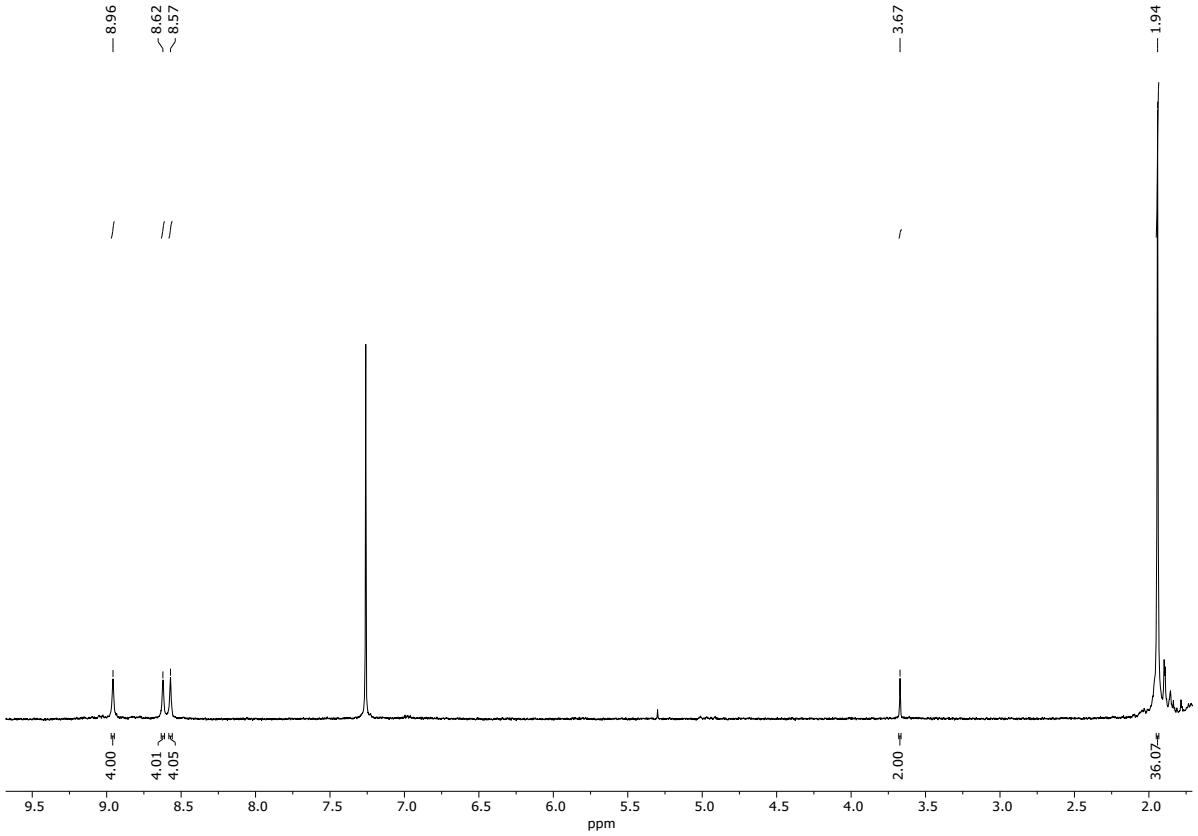

Figure S24. ^{1}H NMR (500MHz, $CDCl_3$) spectrum of compound **HBC-alk.**

HBC-SMe:

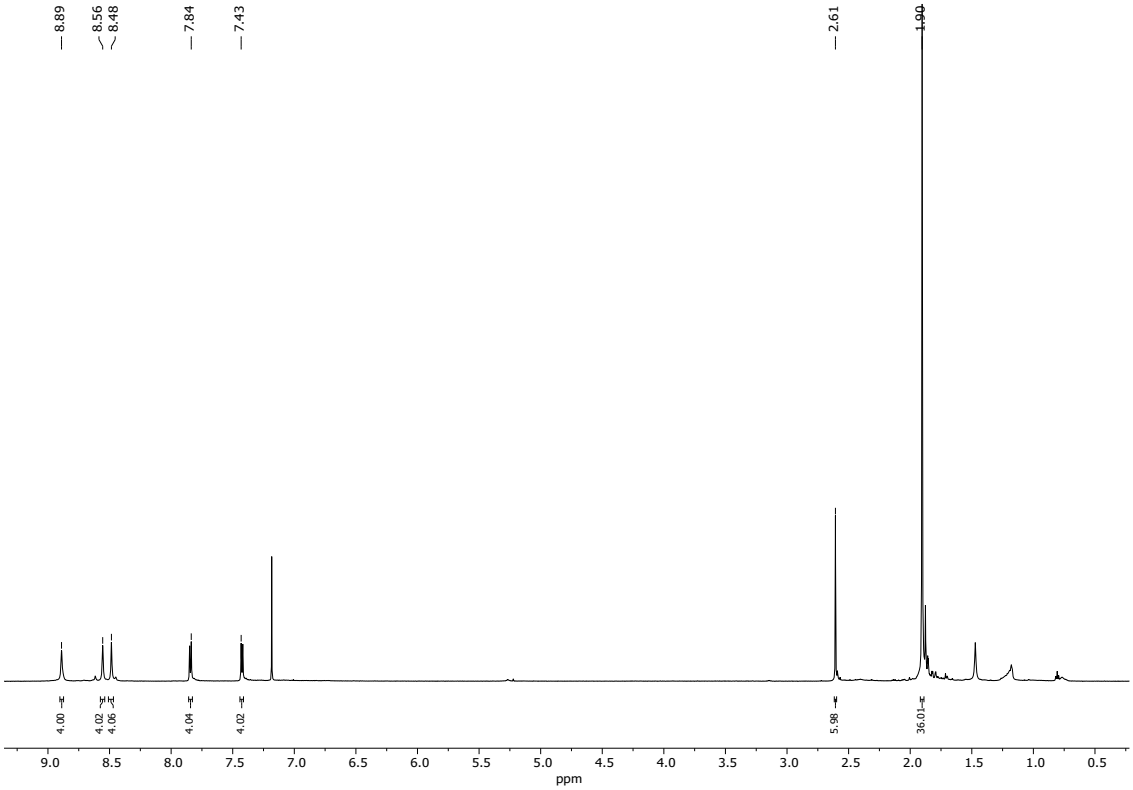

Figure S25. ^{1}H NMR (500MHz, $CDCl_3$) spectrum of compound **HBC-SMe.**

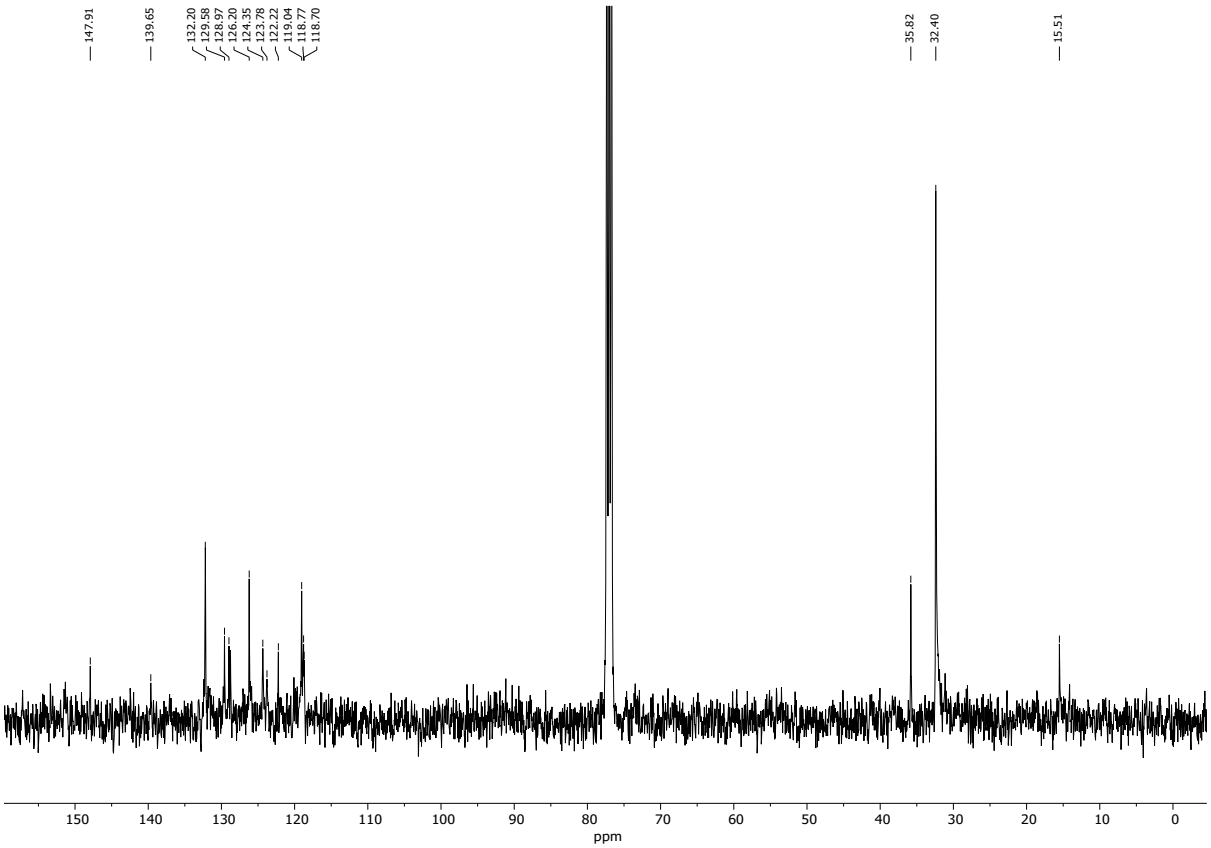

Figure S26. ^{13}C NMR (126 MHz, $CDCl_3$) spectrum of compound **HBC-SMe.**

7-HPB-SMe

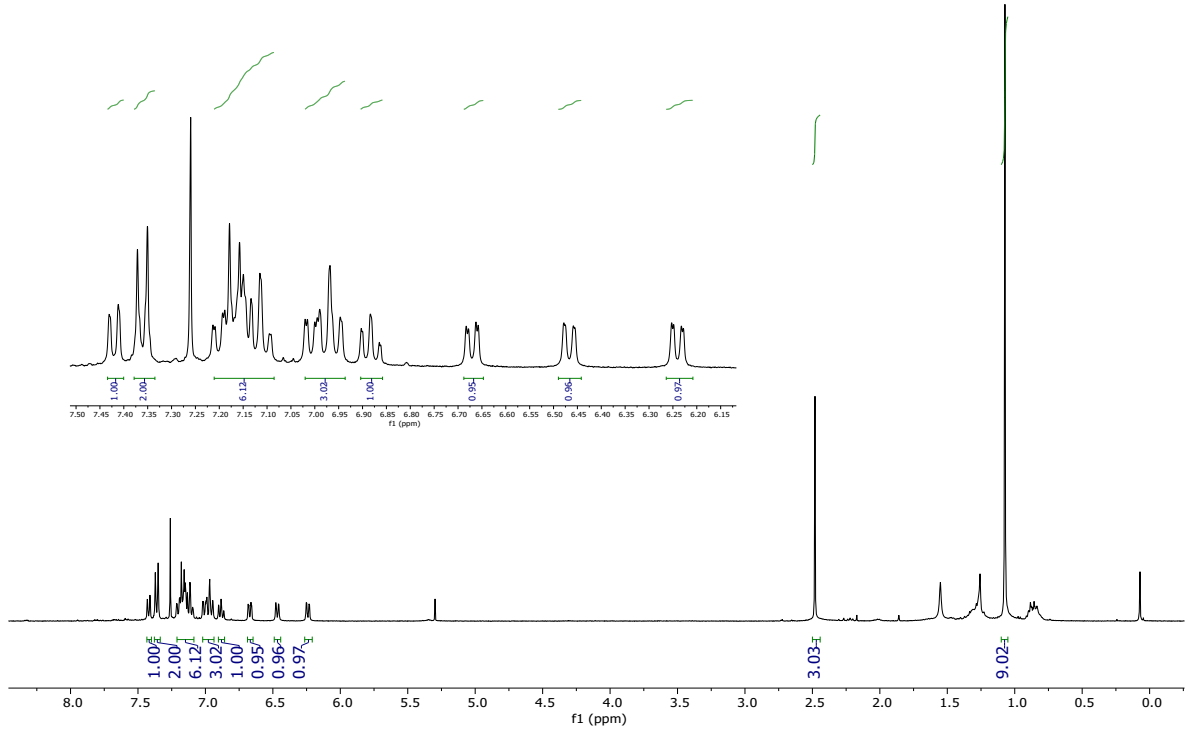

Figure S27. ^{1}H NMR (500 MHz, $CDCl_3$) spectrum of compound **7-HPB-SMe.** Inset: zoom in the aromatic region

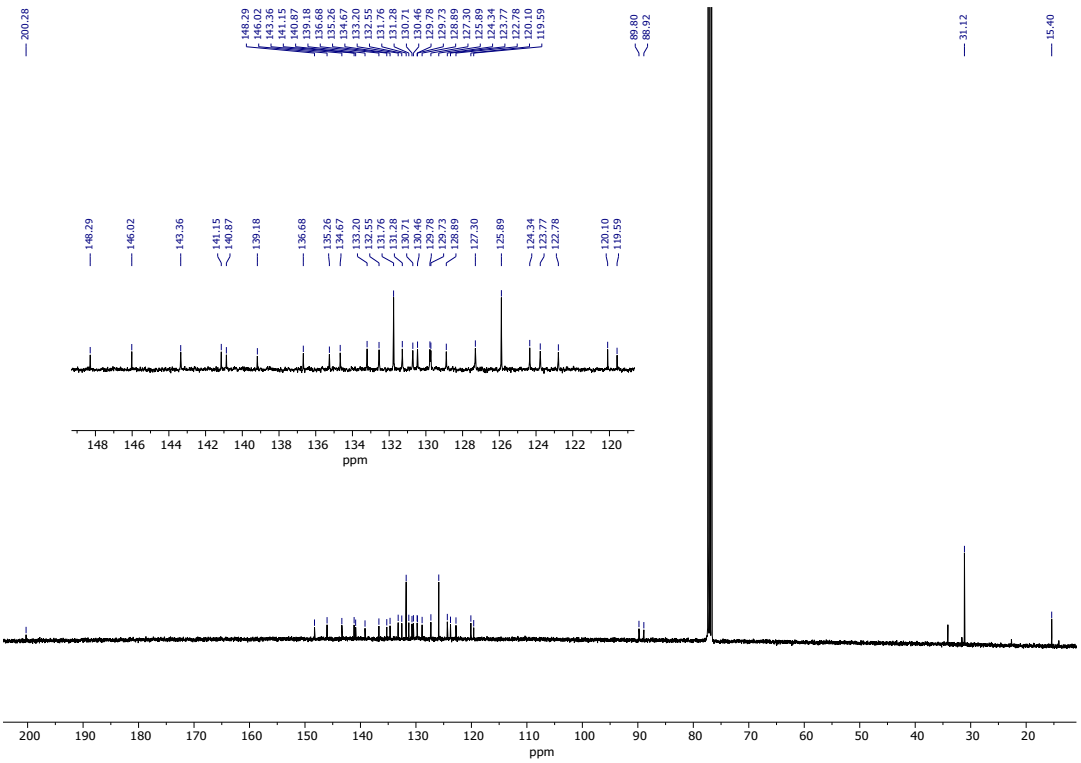

Figure S28. ^{13}C NMR (126 MHz, $CDCl_3$) spectrum of compound **7-HPB-SMe.** Inset: zoom in the aromatic region.

6. References

1 S. Castro-Fernández, C. M. Cruz, I. F. A. Mariz, I. R. Márquez, V. G. Jiménez, L. Palomino-Ruiz, J. M. Cuerva, E. Maçôas and A. G. Campaña, *Angew. Chem. Int. Ed.*, 2020, **132**, 7205–7211.

2 L. Palomino-Ruiz, P. Reiné, I. R. Márquez, L. Álvarez De Cienfuegos, N. Agraït, J. M. Cuerva, A. G. Campaña, E. Leary, D. Miguel, A. Millán, L. A. Zotti and M. T. González, *J. Mater. Chem. C*, 2021, **9**, 16282–16289.

3 M. M. Martin, D. Lungerich, P. Haines, F. Hampel and N. Jux, *Angew. Chem. Int. Ed.*, 2019, **58**, 8932–8937.

4 C. R. Arroyo, E. Leary, A. Castellanos-Gómez, G. Rubio-Bollinger, M. T. González and N. Agraït, *J. Am. Chem. Soc.*, 2011, **133**, 14313–14319.

5 K. B. Dhungana, S. Mandal and R. Pati, *J. Phys. Chem. C*, 2012, **116**, 17268–17273.

6 L. Palomino-Ruiz, S. Rodríguez-González, J. G. Fallaque, I. R. Márquez, N. Agraït, C. Díaz, E. Leary, J. M. Cuerva, A. G. Campaña, F. Martín, A. Millán and M. T. González, *Angew. Chem. Int. Ed.*, 2021, **60**, 6609–6616.

7 A. Magyarkuti, O. Adak, A. Halbritter and L. Venkataraman, *Nanoscale*, 2018, **10**, 3362–3368.

8 D. Miguel, L. Álvarez De Cienfuegos, A. Martín-Lasanta, S. P. Morcillo, L. A. Zotti, E. Leary, M. Bürkle, Y. Asai, R. Jurado, D. J. Cárdenas, G. Rubio-Bollinger, N. Agraït, J. M. Cuerva and M. T. González, *J. Am. Chem. Soc.*, 2015, **137**, 13818−13826.

9 R. C. Hoft, M. J. Ford and V. M. Garc, *J. Phys. Condens. Matter*, 2008, **20**, 025207.

10 E. Leary, L. A. Zotti, D. Miguel, I. R. Márquez, L. Palomino-Ruiz, J. M. Cuerva, G. Rubio-Bollinger, M. T. González and N. Agraït, *J. Phys. Chem. C.*, 2018, **122**, 3211−3218.

11 M. Frei, S. V. Aradhya, M. S. Hybertsen and L. Venkataraman, *J. Am. Chem. Soc.*, 2012, **134**, 4003–4006.

12 G. Mitra, V. Delmas, H. Al Sabea, L. Norel, O. Galangau, S. Rigaut, J. Cornil, K. Costuas and E. Scheer, *Nanoscale Adv.*, 2022, **4**, 457–466.

13 P. Maity, S. Takano, S. Yamazoe, T. Wakabayashi and T. Tsukuda, *J. Am. Chem. Soc.*, 2013, **135**, 9450–9457.

14 R. Ahlrichs, M. Bär, M. Häser, H. Horn and C. Kölmel, *Chem. Phys. Lett.*, 1989, **162**, 165–169.

15 J. P. Perdew, *Phys. Rev. B*, 1986, **33,12**, 8822–8824.

16 A. Schäfer, H. Horn and R. Ahlrichs, *J. Chem. Phys.*, 1992, **97**, 2571–2577.

17 F. Pauly, J. K. Viljas, U. Huniar, M. Häfner, S. Wohlthat, M. Bürkle, J. C. Cuevas and G. Schön, *New J. Phys.*, 2008, **10**, 125019.

18 S. Y. Quek, L. Venkataraman, H. J. Choi, S. G. Louie, M. S. Hybertsen and J. B. Neaton, *Nano Lett.*, 2007, **7**, 3477–3482.

19 L. A. Zotti, M. Bürkle, F. Pauly, W. Lee, K. Kim, W. Jeong, Y. Asai, P. Reddy and J. C. Cuevas, *New J. Phys.*, 2014, **16**, 015004.

20 J. García-Inglés, C. Roldán-Piñero, D. Alejandro Moreno Ramos, R. G. Uceda, J. M. Cuerva, E. Leary, D. Miguel and L. A. Zotti, *J. Phys. Condens. Matter*, 2025, **37**, 135301.

21 R. S. Mulliken, C. A. Rieke, D. Orloff and H. Orloff, *J. Chem. Phys.*, 1949, **17**, 1248–1267.

22 F. A. Van-Catledge, *J. Org. Chem.*, 1980, **45**, 4801–4802.

23 A. Mishchenko, L. A. Zotti, D. Vonlanthen, M. Bürkle, F. Pauly, J. C. Cuevas, M. Mayor and T. Wandlowski, *J. Am. Chem. Soc.*, 2011, **133**, 184–187.

24 E. A. Weiss, G. K. Kaufman, J. K. Kriebel, Z. Li, R. Schalek and G. M. Whitesides, *Langmuir*, 2007, **23**, 9686–9694.

25 L. Cademartiri, M. M. Thuo, C. A. Nijhuis, W. F. Reus, S. Tricard, J. R. Barber, R. N. S. Sodhi, P. Brodersen, C. Kim, R. C. Chiechi and G. M. Whitesides, *J. Phys. Chem. C*, 2012, **116**, 10848–10860.

26 X. Chen, H. Hu, J. Trasobares and C. A. Nijhuis, *ACS Appl. Mater. Interfaces*, 2019, **11**, 21018–21029.